Erosion behavior of CMAS/VA infiltrated EB-PVD Gd$_2$Zr$_2$O$_7$ TBCs: Special emphasis on the effect of mechanical properties of the reaction products

Lars Steinberg[1], Christoph Mikulla[2], Ravisankar Naraparaju[2], Paul Pavlov[3], Markus Löffler[4], Uwe Schulz[2], Christoph Leyens[1,5]

1) Technische Universität Dresden, Institute of Materials Science (IfWW), D-01062 Dresden (Germany)
2) German Aerospace Center (DLR), Institute of Materials Research, D-51170 Cologne (Germany)
3) Anton Paar Germany GmbH, D-73760 Ostfildern, (Germany)
4) Technische Universität Dresden, Center for Advancing Electronics Dresden (cfaed), Dresden Center for Nanoanalysis (DCN), D-01062 Dresden (Germany)
5) Fraunhofer Institute for Material and Beam Technology (IWS), D-01277 Dresden, (Germany)

Declarations of interest: none

Corresponding author: Ravisankar Naraparaju

Email address: Ravisankar.Naraparaju@dlr.de

Phone: +49 2203 601-3442

Postal address: Deutsches Zentrum für Luft- und Raumfahrt e. V. (DLR)

Linder Höhe

51147 Köln

Erosion behavior of CMAS/VA infiltrated EB-PVD $Gd_2Zr_2O_7$ TBCs: Special emphasis on the effect of mechanical properties of the reaction products

Lars Steinberg[1], Christoph Mikulla[2], Ravisankar Naraparaju[2], Paul Pavlov[3], Markus Löffler[4], Uwe Schulz[2], Christoph Leyens[1],[5]

6) Technische Universität Dresden, Institute of Materials Science (IfWW), D-01062 Dresden (Germany)
7) German Aerospace Center (DLR), Institute of Materials Research, D-51170 Cologne (Germany)
8) Anton Paar Germany GmbH, D-73760 Ostfildern, (Germany)
9) Technische Universität Dresden, Center for Advancing Electronics Dresden (cfaed), Dresden Center for Nanoanalysis (DCN), D-01062 Dresden (Germany)
10) Fraunhofer Institute for Material and Beam Technology (IWS), D-01277 Dresden, (Germany)

Declarations of interest: none

Corresponding author: Ravisankar Naraparaju

Email address: Ravisankar.Naraparaju@dlr.de

Phone: +49 2203 601-3442

Postal address: Deutsches Zentrum für Luft- und Raumfahrt e. V. (DLR)

Linder Höhe

51147 Köln

Abstract

Aero-engines operating in sand-laden (CMAS/CaO-MgO-Al_2O_3-SiO_2) environments often encounter severe problems with thermal barrier coatings (TBCs) due to CMAS infiltration and erosion damage. This study focuses on a deeper understanding of the erosion behavior of CMAS-infiltrated EB-PVD $Gd_2Zr_2O_7$ TBCs. The study includes isothermal infiltration of different CMAS and subsequent erosion tests at room temperature.

In addition to the erosion behavior of the entire coating, the influence of different reaction products within the reaction layer on erosion failure was investigated by measuring the hardness and Young's modulus of the individual phases using in-situ REM-Nanoindentation. It was found that a garnet layer above the reaction layer and spinel inclusions within a thick apatite/fluorite reaction layer, can improve the erosion resistance of this reaction layer by 30-40%. Furthermore, a correlation between the erosion behavior and the hardness vs. Young's modulus relation, obtained from nanoindentation over the entire coating, was observed for a consistent microstructure.

Keywords: $Gd_2Zr_2O_7$; CMAS; TBC, Erosion, EB-PVD

1. Introduction

The application of thermal barrier coatings (TBC) within the turbine leads to an increase in its thermal load limit to over 1400 °C (1, 2). The TBC systems are applied by electron beam physical vapor deposition (EB-PVD) or atmospheric plasma spraying (APS) on the nickel-based superalloy of the turbine blade or combustion chamber (3-5). Due to the low thermal conductivity of TBC, a temperature gradient (T-gradient) of at least 100 K can be achieved over several hundred micrometers of coating thickness .In addition to yttrium oxide partially stabilized zirconium oxide (e. g. 7YSZ) as the industry standard, research is currently being conducted on alternatives with even lower specific thermal conductivity coefficients, so-called low-k TBCs (6-14).

The most intensively studied representative of these low-k TBCs is $Gd_2Zr_2O_7$ (GZO)(15-17). The advantage of the GZO is the lower thermal conductivity compared to 7YSZ. Furthermore, the characteristic pyrochlore phase is stable up to 1550 °C and shows a low sintering tendency at elevated temperatures. However, the lower coefficient of thermal expansion of the GZO leads to high residual stresses in the bond coat/TBC interface which, in combination with the lower fracture toughness, can lead to premature failure of the layer (8, 18, 19). Due to the use of aircraft engines in sand or volcanic ash rich areas, particles enter the turbine, causing erosive damage and CMAS-corrosion to the TBC at high turbine inlet temperatures (20-23). In case of CMAS infiltration the stiffening of the columns leads to a loss of strain tolerance of the EB-PVD TBC, whereby thermal shock scenarios can lead to coating failure due to the residual stresses which are now present. Furthermore, a dissolution/re-dissolution process of the column material as well as an increase of the thermal conductivity takes place. To prevent CMAS infiltration, current research focuses on so-called sacrificial layers of e.g. GZO, Al_2O_3, 65YZ, etc.(19, 24-30).The principle of sacrificial layers is to form quickly a protective reaction layer during CMAS infiltration which consists of new crystalline phases with higher melting points. This layer inhibits further CMAS infiltration into the TBC. These high-temperature stable phases, such as apatite, fluorite, garnet, zirconium, and especially spinel (in case of an Al_2O_3 sacrificial layer (31)), block the infiltration paths of the CMAS and serve as a barrier against further CMAS infiltration. Therefore, the further infiltration of CMAS into the underlying unreacted coating is inhibited.

The effectiveness of this barrier effect depends on a complex interaction of different factors, which have been studied for GZO layers in (17, 21, 26, 32). All GZO reaction layers, formed during the infiltration of a CMAS with a low basicity index, consist of the same phases: apatite, fluorite, spinel, garnet, and zirconolite. Only the relative proportions of the phases vary due to the different quantities of available elements in the CMAS and therefore influences the microstructure of the respective reaction layers. In the case of GZO TBC, it is known from many studies that the reaction product apatite meets the kinetic and thermodynamic requirements and thus its formation is essential for the high resistance of GZO against CMAS infiltration. It is known that apatite is the very first reaction product that forms upon CMAS reaction and seals the inter-columnar porosity against further melt infiltration. Other reaction products such as spinel, anorthite, fluorite do not show any protection against CMAS infiltration rather they are present as a byproduct (26). However, GZO and VA reactions show that the apatite stability is questionable after longer infiltration times and necessitates other protection strategies (33). Similarly, it was shown by the authors that a continuous garnet formation on top of GZO as a reaction layer was

found to be very useful in restricting the GZO consumption and highly dependent on the chemical composition of the CMAS (26).

In contrast to CMAS infiltration, the erosive coating damage is dominated by cracks. Therefore, fracture toughness, Young's modulus and hardness are the most important properties for assessing erosion resistance (34). Due to the comparatively high fracture toughness of t'-7YSZ (K_{IC}=1.8-4.5 MPa·m$^{1/2}$) (35), this material currently has the highest erosion resistance of all TBC coatings (36). GZO, as a representative of low-κ TBC, only achieves a K_{IC} of 1.0 MPa·m$^{1/2}$(37). In the case of single layer GZO TBC and GZO/YSZ multilayer TBC, Mahade et al. (38) showed that, despite the higher porosity of the YSZ reference sample, YSZ has a significantly higher erosion resistance than the GZO (multilayer) coatings.

Previous research has considered the two damage mechanisms, CMAS infiltration, and particle erosion, mostly as separate, independent processes. Wellman et al. (34, 39-41) and numerous other research groups (37, 38, 42, 43) investigated the erosion behavior of TBCs at room temperature (RT) and high temperatures (HT). The mechanical and chemical effects of CMAS infiltration on TBCs were also investigated in detail (3, 21, 44). However, both mechanisms occur alternately or even simultaneously during the life cycle of TBCs. So far, only a few studies (40, 41, 45, 46) have considered the change in the erosion behavior of a TBC after CMAS infiltration. In one of our previous studies (46) the erosion behavior of a CMAS infiltrated TBC system (SPS Alumina layer: a sacrificial layer) was studied.

The current study deals with the erosion behavior of CMAS-infiltrated EB-PVD GZO TBCs at RT. Besides the influence of the infiltration depth on the erosion behavior, the focus of this study is on the erosion behavior of the GZO reaction layer. The chemistry of CMAS as well as the infiltration time has shown a big influence on the erosion resistance of EB-PVD 7YSZ in previous studies by the authors (45,46). Therefore, two CMAS and one natural Iceland volcanic ash were used for short-term and long-term infiltration tests on EB-PVD GZO TBCs. The influence of CMAS chemistry on the reaction layer formation of EB-PVD GZO was studied in detail and is not presented here. Nanoindentation measurements were performed to determine the course of the local mechanical properties over the infiltrated coating systems and individual reaction phases and to correlate with the changing erosion rates. This provides a basis for the interpretation of the influence of the chemical and mechanical aspects of the CMAS infiltration on the erosion behavior. The comparison between 7YSZ and GZO erosion behavior is currently in progress and will be published separately.

2. Experimental procedure

2.1. Coating system

The tested TBCs were produced by the EB-PVD process at the DLR, Cologne. The process parameters for the 326-358 µm thick GZO TBC involved a substrate temperature of approx. 975 °C, a pressure of 6 x 10^{-3} mbar, and a rotation speed of 12 min^{-1}. Due to the subsequent isothermal annealing and CMAS infiltration at elevated temperatures of 1250°C, which exceed the operational temperature limits of Ni-based substrates and NiCoCrAlY bond coats, a (34x20x1) mm³ densified, sintered Al$_2$O$_3$ plate was used as a substrate material for the TBCs. The columns are bent by up to 10° in the area close to the substrate (50).

2.2. CMAS infiltration

Two synthetic CMAS compositions (derived from real engine deposits operated in middle-east region (20) and Iceland volcanic ash (VA, Eyjafjallajökull ash was collected at 63°40'42.10"N; 19°37'31.75"W about 4 km from the source (48) were used for the infiltration tests at DLR. Further information regarding the chemical composition and other characteristic properties can be found in Table 1. The CMAS/VA powder was converted into a paste by adding water. The CMAS paste was then applied onto the TBC at a concentration of 10 mg/cm² and air-dried at ambient temperature.

Table 1   Summary of CMAS and VA compositions in mol.-%, melting range, viscosity, basicity index (BI) and main phases based on data of (20, 29, 47-49).

Chemical composition in mol.-%								Metling range in °C	Viscosity in Pa·s	BI	Main phases
SiO$_2$	CaO	MgO	Al$_2$O$_3$	FeO	TiO$_2$	Na$_2$O	K$_2$O				

										(1250 °C)		
VA (VA)	49.7	12.5	6.0	7.4	17.6	4.3	2.0	0.4	1060-1150	250	1.0	Amorphous
CMAS 1 (C1)	41.6	24.7	12.3	11.1	8.7	1.6	-	-	1230-1250	6.9	1.4	Pyroxene, Anorthite
CMAS 2 (C2)	37.3	32.4	11.2	9.9	7.8	1.4	-	-	1215-1245	4.0	1.7	Pyroxene, Melilite

The isothermal CMAS infiltration was then carried out in a box furnace at 1250 °C for 300 min for the short-term infiltration tests and 3000 min for the long-term infiltration tests. As a result of the different durations of infiltration, different infiltration depths and reaction layer thicknesses were obtained, which made it possible to analyze their influence on the erosion properties of the infiltrated TBCs. To study the erosion properties of the reaction products such as garnet, apatite, spinel and fluorite, a thick reaction layer would be necessary and 50 h infiltration time was selected rather than shorter infiltration times. The investigated GZO TBCs were heated up and cooled down in a controlled process at rates of 10 K/min. Additionally, GZO TBCs without CMAS deposition were aged for 3000 min at 1250 °C to investigate the sintering effect of this heat treatment on the GZO TBC structure and its erosion behavior. In order to precisely describe the numerous experiments, a particular nomenclature is used depending on the type of infiltration history that is presented in Table 2.

Table 2   Tested GZO EB-PVD samples with variations in CMAS compositions and heat treatment

Sample designation	Type of CMAS	Duration of heat treatment in min
NI/0	-	-
NI/3000		3000
VA/300	Iceland VA	300
VA/3000	Iceland VA	3000
C1/300	CMAS 1	300
C1/3000	CMAS 1	3000
C2/300	CMAS 2	300
C2/3000	CMAS 2	3000

2.3.   Erosion tests

The erosion tests were carried out at room temperature in an erosion test rig at the Technische Universität Dresden. The erosion parameters were identical to those from (45,46). Al_2O_3 particles with a size distribution of 54.5 µm (d10), 92.5 µm (d50), and 142.7 µm (d90) (Cilas, Cilas 1064) were used at a feeding rate of 0.25 g/min (powder feeder GTV PF2/1, GTV Verschleißschutz GmbH). After the acceleration of the particles through a focused high-pressure gas stream, mean particle velocities of 125 m/s were achieved (measured with PIV system, PyroOptic Aps). These particles impinged on the TBC surface at an angle of 45° or 90°, depending on the experimental setup. The distance between the nozzle and the sample was adjusted at 30 mm. The samples were weighed before the erosion test and after each erosion interval (Mettler Toledo Analytical Balances XA105DU). The short intervals of 15 s within the first 240 s of the erosion test were used to visualize in detail the removal of the reaction layers. After 240 s, longer erosion intervals (60 s) followed to minimize the measurement error and thus enabled a more precise determination of the erosion rate. Due to the different densities of the non-infiltrated and infiltrated GZO TBCs, additional confocal microscope measurements (NanoFocus, µscan) were carried out before, during, and after the erosion test to determine the erosion volume.

The 3-D Gaussian distribution of the eroding particles in the particle stream leads to a more concentrated erosion in the center of the erosion spot. In the case of erosion of multi-region systems (e.g. reaction layer, infiltrated GZO TBC, non-infiltrated GZO TBC) this leads to a complex erosion situation which makes it difficult to separate the effects of the different layers. As soon as the first layer in the center of the erosion spot is removed, the next, now exposed layer starts to erode, while in the outer area of the erosion spot the first layer continues to be eroded. This is due to the locally lower particle flow in the outer area compared to the center of the erosion spot, which results in a lower local removal of the coating volume per erosion interval in the outer area. This leads to concentric circles for each layer, which grow in diameter over time. In the case of erosion at an angle of 45°, the individual layer is removed more slowly, which allows a more precise determination of the erosion resistance of each layer. The nomenclature of the erosion tests is presented in Table 3.

5

Table 3   Nomenclature of the erosion tests.

Designation of erosion test	Erosionmode	Particle impact angle
E/90	Erosion Mode	90°
E/45		45°

The constant erosion rate of the GZO TBC is determined according to standard procedures by measuring the weight changes. The comparison of the GZO erosion behavior with the 7YSZ TBC and other literature data is described in detail in (50). Nevertheless, due to the varying thicknesses of the reaction layers and the varying degrees of CMAS infiltration below the reaction layers, the determination of a characteristic, constant erosion rate is largely affected by errors. However, the erosion processes can be emulated more precisely by a cubic fit. The first derivation of the respective cubic function, the erosion rates are plotted over the erosion time. This novel kind of evaluation of the erosion rate makes it possible to correlate the rate with the changing erosion mechanisms and furthermore, with the mechanical data of the complete coating structure, especially that of the reaction layer (for more details see (50)).

2.4.   Measurements of mechanical properties

The NHT³ nanoindentation tester from Anton Paar was used to identify the local layer properties of the GZO coatings. The measurements were performed with a Berkovich diamond tip in an array of at least 8x10 indentations (8 indentations per coating depth) on the cross-sections of the coating. To minimize this influence of bending columns and at the same time to achieve reliable penetration depths with consistent measurement values, the nanoindentation measurements were conducted at a force of 250 mN. More detailed information are given in (50).

The determination of the GZO reaction layer properties was complemented by the indentation of the individual phases. The necessary in-situ SEM nanoindentation (SEM: FEI Helios NanoLab 660; picoindenter: PI87, Bruker/Hysitron®) was performed with a Berkovich diamond tip at 4 mN (load speed of 9.6 mN/min; holding time of 10 s). The statistical validation of these measurements is 3-5 measuring points per phase. This technique is applied here for the first time in the CMAS related research.

Based on investigations by Jackson et al. (19), which were also performed on CMAS-infiltrated GZO samples, a Poisson ratio of 0.2 was used to calculate the nanoindentation values for CMAS-infiltrated GZO.

2.5.   Microstructural characterization

The samples were analyzed under a scanning electron microscope (SEM: DSM 982 Gemini, Zeiss, Germany). The CMAS infiltration zone as well as the reaction phases were identified by analyzing the SEM-images in combination with energy dispersive X-ray-analysis (EDX: Noran System 7, Thermo Scientific). The erosion damage of the coatings was investigated in SEM images taken after the erosion test.

3. Results

3.1.   Microstructural characterization of EB-PVD GZO coating before and after CMAS infiltration

Both the column diameter and the inter-columnar gap widths of GZO coating increased from bottom to the top with an average columnar gap of 2.1 µm in the top region (Fig. 1 a). To analyze the sintering influence on the erosion behavior, a heat treatment at 1250 °C/3000 min was performed. The incipient sintering mechanisms, which reduce the (open) porosity of the columns, can be seen at the microstructure in Fig. 1 b) by looking at the coalescing feather arms. The characteristic sintering of the columns described by Wellman et al. (39) and this allows crack propagation across multiple columns, was not detected in the upper coating region. The absence of sintered columns might be attributed to the large gaps between the GZO columns and in that consequence the lack of material contact between the columns. Due to the sintering process the inter-columnar gaps increase after the NI/3000 heat treatment (see Fig. 1 a-b). Measurements of the gap widths by ImageJ, which are not shown here, confirmed an increase of these gaps by approx. 80 % at a coating depth of circa 70 µm.
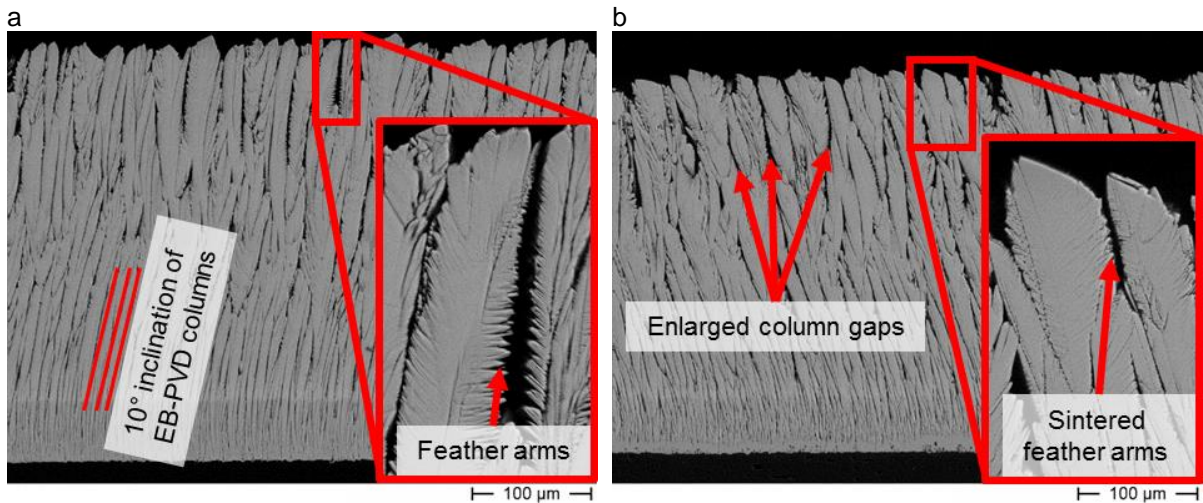
Fig. 1   SEM image of non-filtered GZO samples showing column bending in the lower part and approx. 10° column inclination at a) NI/0 and sintering effects at b) NI/3000.

Reaction layer formation and the infiltration behavior of different CMAS compositions in GZO:

In the following, the different reaction layers and CMAS-infiltration depths due to the different CMAS compositions will be discussed:
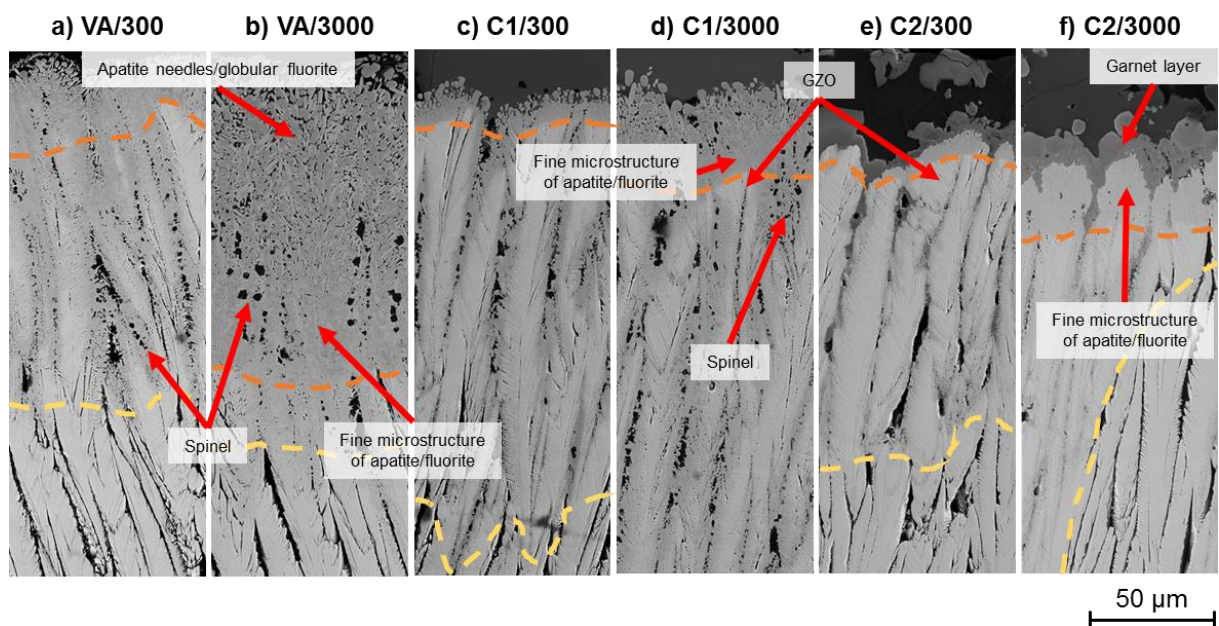

Fig. 2   SEM image of characteristic reaction layer formation and infiltration behavior into the GZO TBC as a function of CMAS composition and infiltration time. The interfaces of reaction layer/CMAS infiltrated GZO (orange) and CMAS infiltrated/non-infiltrated GZO (yellow) are identified/marked by the dashed lines.
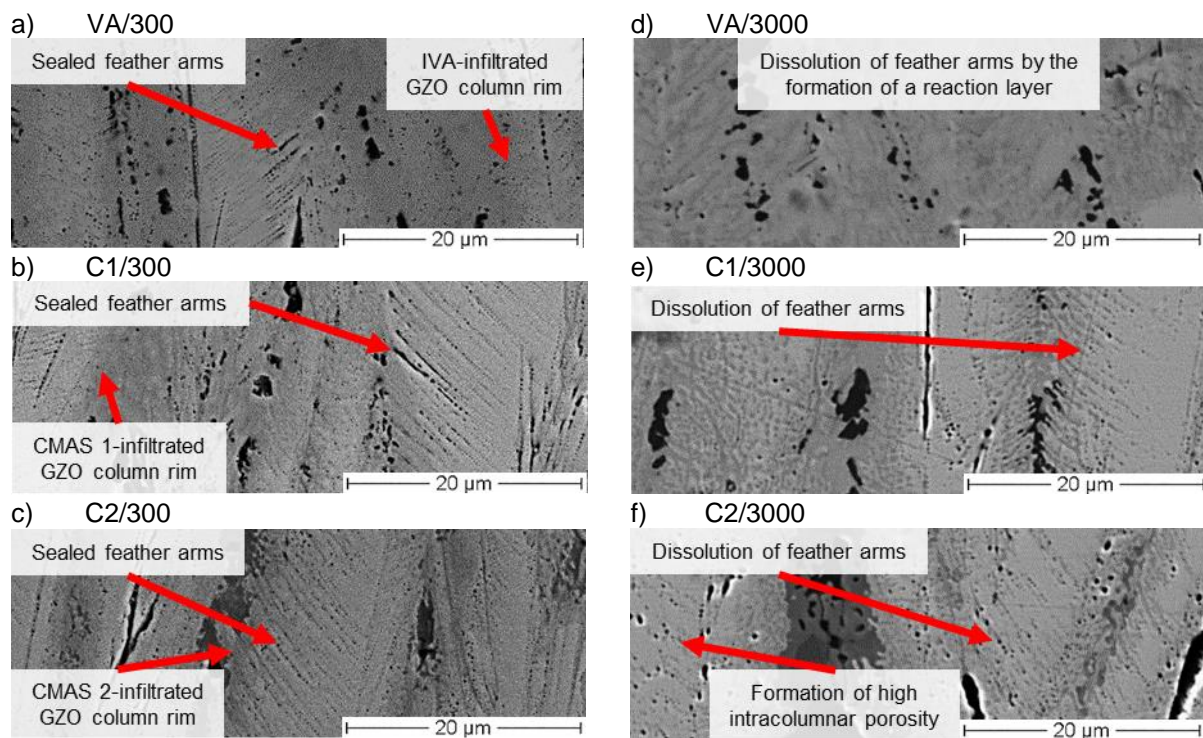
Fig. 3   SEM image of the GZO microstructure after 300-/3000-minute infiltration at a coating depth of circa 60 μm, considering the infiltration depth of the CMAS along the feather arms, a-c) showing the enlarged pores of the former gaps between the feather arms as well as d-f) the associated dissolution of these feather arms.

Fig. 2 shows the SEM cross-sectional micrographs of different CMAS/VA infiltrated EB-PVD GZO coating at 1250°C after 5 and 50 h. Fig. 3 depicts the infiltration situation at a few microns underneath the top region of infiltrated GZO in high magnification.

The VA infiltrates along the inter-columnar gaps and deep into the feather arms (see Fig. 3 a), leading to rapidly dissolved column tips (see Fig. 2 a-b). Infiltration depth has increased from 145 μm to 170 μm from 300 to 3000 min. I.e. VA reaches approximately 50 % of the coating thickness. After an infiltration time of 3000 min, a complete dissolution of the column structure occurs down to a coating depth of approx. 120 μm (32 μm after 300 min). Above the former GZO columns, Fe/Ti-rich zirconolite is formed. A reaction layer consisting of apatite needles as well as globular fluorite along with the VA residue (up to 10/75 μm after 300/3000 min) was found at the surface. With the increasing infiltration depth, the apatite and fluorite grains become finer and form a finely distributed two-phase microstructure. In addition, the remaining Fe-oxide along with MgO and aluminum oxide present in the melt (between the fine apatite/fluorite crystals) form spinel as shown as dark crystals (Fig. 2 a-b) (26). The intense infiltration of the feather arms (see Fig. 3 a & d) increases the GZO/VA interface and consequently the extent of reaction. Furthermore, the high viscosity of VA (see Table 1) causes slow infiltration, providing the necessary time for the GZO to react with VA toward HT-stable phases (e.g. apatite).

CMAS 1 exhibits the deepest infiltration among the other used compositions. In contrast to VA, due to the lower viscosity of CMAS 1 (see Table 1), faster infiltration took place and a thinner reaction layer was observed. The infiltration depth reaches approx. 165 μm after 300 min and a complete infiltration of approximately 330 μm after 3000 min. It forms a 15 μm thin reaction layer consisting of apatite and fluorite crystals after 300 min, which grows up to 46 μm after 3000 min. The microstructure of the CMAS 1 reaction layer, shown in Fig. 2 c-d, is similar to VA-infiltrated GZO samples, but much thinner after 3000 min. This reaction layer consists of coarse apatite as well as globular fluorite crystals in the upper region and changes into a fine two-phase apatite/fluorite microstructure with spinel inclusions as the CMAS infiltrates deeper. Inhomogeneous large garnet domains which consumed larger amounts of CMAS residue, interspersed with isolated spinel grains, form above the apatite/fluorite at the TBC/melt interface. The feather arms were partially infiltrated after 300 min (see Fig. 3 b) and sealed by the formation of apatite phase. This microstructure prevails even after 3000 min (Fig. 3 e) unlike in the case of VA.

8

The mean infiltration depth of CMAS 2 of approx. 150 µm after 300 min is comparable to that of VA (50). After 3000 min, the infiltration depth increases again, with great local variation between 170 µm and complete infiltration (50). The reaction layer does not contain acicular apatite or globular fluorite grains but consists of a fine two-phase apatite/fluorite microstructure (reaction layer thickness: 16/28 µm after 300/3000 min). In contrast to the reaction layers described previously, CMAS 2 forms a continuous garnet layer (26), which grows from 7 µm (300 min) to 18 µm (3000 min) (see Fig. 2 e-f). All the phases that were identified using SEM (EDS) studies were compared with our previous results where Transmission Electron Microcopy (TEM) and X-ray diffraction (XRD) techniques were applied to identify the reaction products.
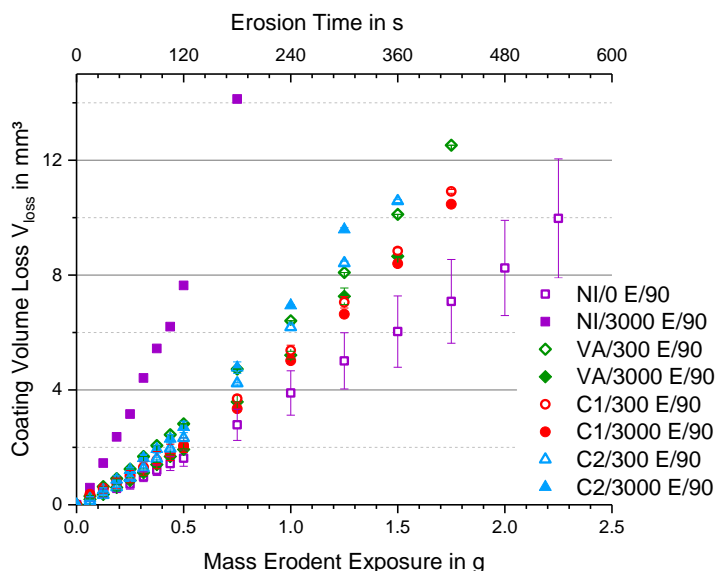
3.2.   Erosion results

a
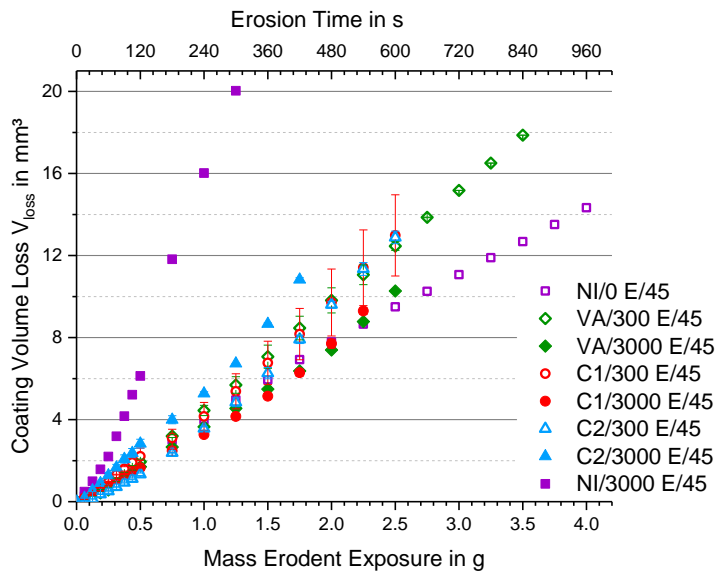
b

Fig. 4   Erosion data of non-infiltrated and infiltrated EB-PVD $Gd_2Zr_2O_7$ after short-/ and long-term infiltrations for a) E/45 and b) E/90.

Influence of heat treatment/infiltration time on erosion behavior of non-infiltrated GZO TBCs

Due to the high sintering resistance of GZO, the extended heat treatment of 3000 min was used to validate the sintering effect on erosion behavior for GZO TBCs. While the NI/0 samples achieved erosion

rates up to 4.8 mm³/g (E/90; after 360 s) and 4.1 mm³/g (E/45; 30 s-105 s), the rate increased to 21.1 mm³/g (E/90; after 120 s) and 21.5 mm³/g (E/45, after 180 s) for NI/3000 (see Fig. 5). After the NI/3000 heat treatment, these samples reached the highest erosion rates of all GZO TBCs.

In contrast to the EB-PVD 7YSZ TBCs, in general, a trend has been observed that the erosion rate increased after CMAS infiltration regardless of the infiltration time (300 min; 3000 min) compared to NI/0 for all GZO coatings. Fig. 5 a-b) shows the results for E/90 and E/45 of CMAS1 and VA, where the erosion rate after a short-term infiltration was found to be consistently higher compared to the long-term infiltration. CMAS 2, in contrast, is the exception and reaches a higher erosion rate after 3000 min of infiltration.

Influence of CMAS/Island VA composition on the erosion behavior of infiltrated GZO TBC

Concerning the complete erosion process of the entire GZO coating, CMAS 2 experiences the highest erosion rate, followed by VA and CMAS 1 (see Fig. 5). The influence of the CMAS composition on the erosion behavior of the reaction layers can be extracted by analyzing the erosion data of the short-time erosion intervals (erosion time: 0-120 s) as shown in Fig. 5 c-d. For instance, it is shown at E/90 that C2/300 exhibits a low erosion rate of 1.9-3.4 mm³/g at the beginning of the erosion tests (0-30 s). While the erosion rate increases significantly to 4.1-4.8 mm³/g for C2/3000, the reaction layer becomes more erosive resistant after a 3000 min infiltration by VA (1.7-3.0 mm³/g) (compare 0-30 s of VA/300: 5.5-5.7 mm³/g). CMAS 1, in contrast, is less affected by infiltration time (C1/300: 3.7-4.1 mm³/g; C1/3000: 3.1-3.6 mm³/g) and demonstrates moderate erosional behavior within the first 30 s of the erosion test. In the later stages of the initial erosion rate (30-120 s), however, CMAS 1 achieves the lowest erosion rates of all CMAS compositions, relative to the respective infiltration time (see Fig. 5 c-d).

Influence of the particle impact angle on the erosion behavior of the GZO TBC

The tendencies of the erosion behavior, described in the previous section for E/90, were in good agreement with the E/45 tested samples (Fig. 5). The erosion rate increases with an increasing incidence angle of the erosion particles for both the non-infiltrated (e. g. NI/0 E/45: 3.5 mm³/g vs. E/90: 4.5 mm³/g) and infiltrated (e. g. C1/3000 E/45: 3.8 mm³/g vs. E/90: 6.7 mm³/g) GZO TBCs. Since a more extensive removal of the brittle CMAS residue occurs due to the larger erosion spot for the E/45, this trend is in some cases not reached until the first 60 s of the erosion test (see Fig. 5 c-d). In contrast to a previous study on reaction layers (46), the removal of CMAS could be resolved for the first time in the initial erosion phase due to the shortened erosion intervals for the GZO layers and different incidence angles. Unlike the infiltrated GZO E/90, the erosion curve for E/45 is often characterized by a decreasing erosion rate in the first phase of the erosion test, which increases again in the later course (see Fig. 5 a). The characteristic of this parabolic shape increases with increasing infiltration time.
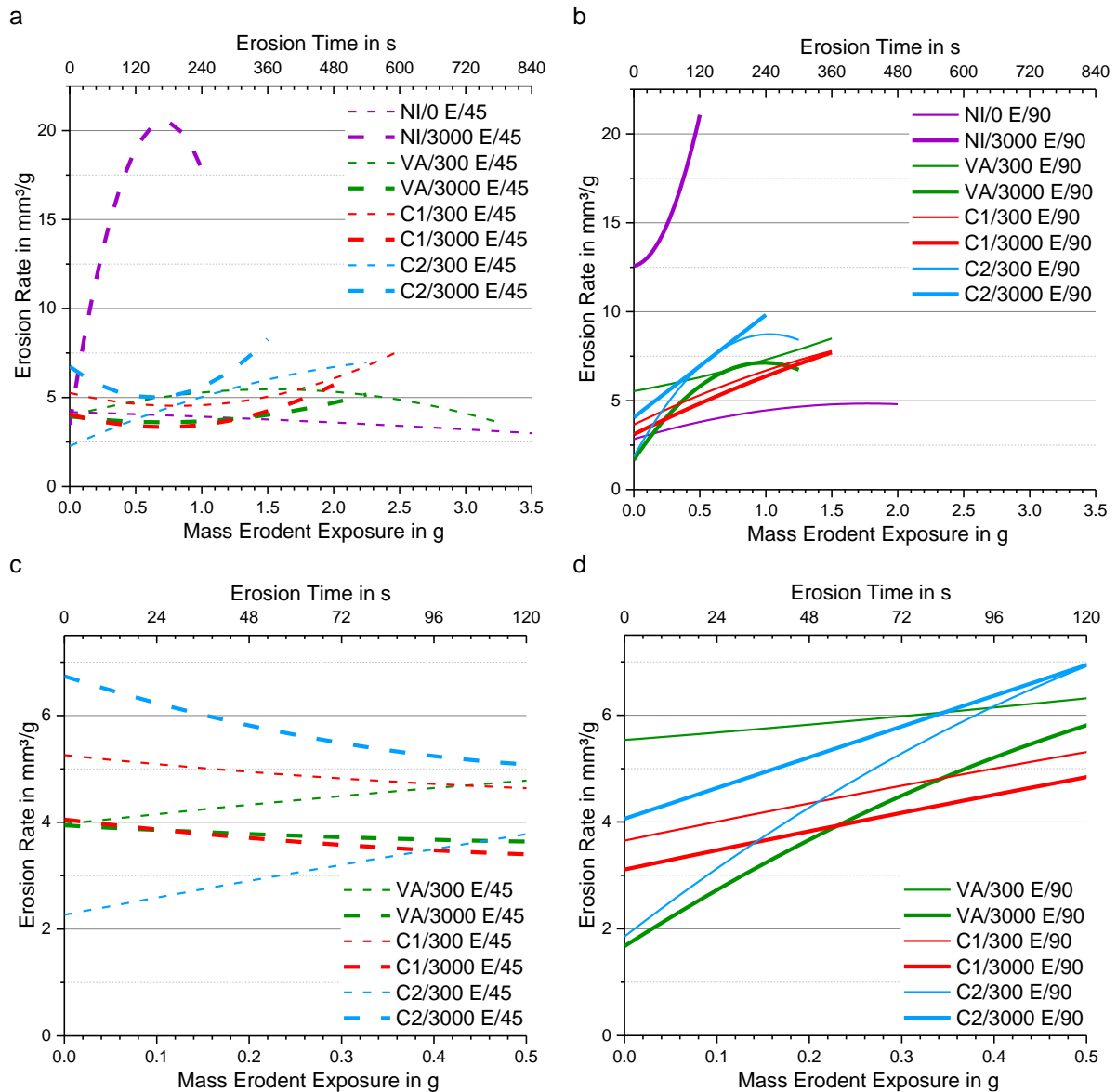
Fig. 5   Erosion rates of GZO samples plotted versus erodent/erosion time after short/ and long term infiltrations for a) E/45; b) E/90; and the first 120 s of erosion time to analyze the reaction layer behavior of infiltrated c) E/45 and d) E/90 (based on the first derivative of the cubic fit of the erosion curves in Fig. 4).

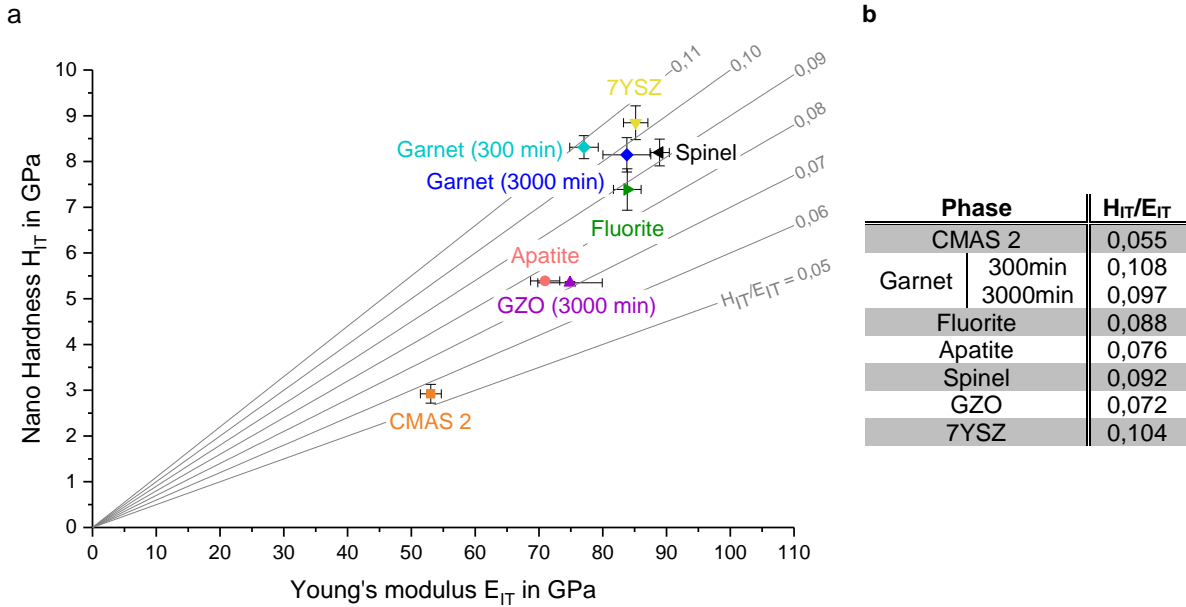## 3.3. Nano hardness and Young's modulus of the reaction phases

a

b

Phase		H_{IT}/E_{IT}
CMAS 2		0,055
Garnet	300min	0,108
	3000min	0,097
Fluorite		0,088
Apatite		0,076
Spinel		0,092
GZO		0,072
7YSZ		0,104

Fig. 6   a) the plot of nano hardness (H_{IT}) versus Young's modulus (E_{IT}) of reaction phases, GZO, CMAS 2 and additionally 7YSZ as reference material measured at an indentation force of 4 mN on VA/3000, C2/3000, C2/300 and a 7YSZ EB-PVD TBC; the grey lines crossing the zero point represent various H to E ratios b) values of the H_{IT}/E_{IT} of the phases.

The mechanical properties of E_{IT} and H_{IT} of the main phases of the GZO reaction layers, as well as of EB-PVD GZO, 7YSZ, and CMAS 2 were measured using in-situ SEM nanoindentation (Bruker/Hysitron PI87, Berkovich tip) (see Fig. 6). In a comparison of the two TBC materials 7YSZ (H_{IT}=8.9 GPa; E_{IT}=85 GPa) has higher values than GZO (H_{IT}=5.4 GPa; E_{IT}=75 GPa) which reflect the superior erosion properties of the 7YSZ. Garnet, spinel, and fluorite achieve the highest values with H_{IT}=7.4-8.3 GPa and E_{IT}=77-89 GPa. The lowest values were measured at CMAS 2 with H_{IT}=2.9 GPa and E_{IT}=53 GPa. The properties of zirconolite phase were not measured as it forms only in small quantities, dispersed discontinuously at the TBC-CMAS interphase inside the brittle CMAS residue. Thus, it has a limited relevance to the erosion behavior.

According to the data from (34, 51), a higher nano hardness and a lower Young's modulus were assumed to have a positive influence on the erosion behavior, i. e. a lower erosion rate. This influence can be discussed by referring to the H_{IT}/E_{IT} ratio also presented in Fig. 6. It can be seen that the 7YSZ as well as the reaction phases garnet and spinel have a high H_{IT}/E_{IT} and can therefore potentially contribute to low erosion rates. The interaction between the mechanical properties of individual phases and the coating properties is described in section 3.4. Based on this, these results allow discussing the influence of the mechanical properties of the reaction layers in correlation with the erosion behavior of the reaction layers for the first time (see section 4.3).
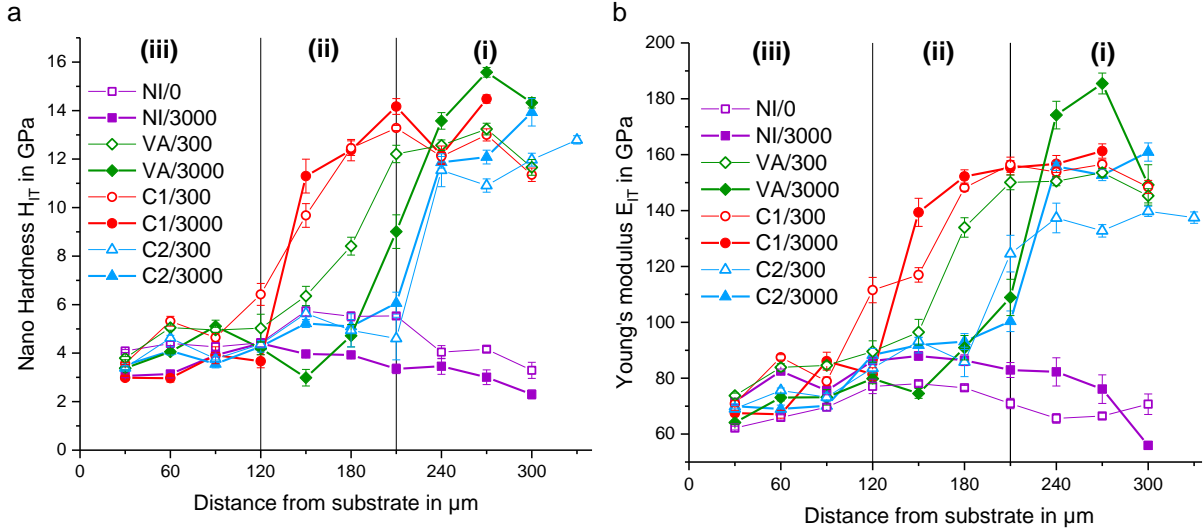
3.4. Nano hardness and Young's modulus over the coating

a

b

Fig. 7   The plot of (a) nano hardness (H_{IT}) and (b) Young's modulus (E_{IT}) of GZO TBCs at an indentation force of 250 mN as a function of TBC thickness (starting from the substrate), partitioned into three representative regions: (i) upper coating region/reaction layer, (ii) middle coating region, and (iii) lower coating region.

The nano hardness and Young's modulus over the entire GZO coatings were measured using Anton Paar's NHT³ nanoindentation tester. The measured values over the entire coating depth are divided into three sections in Fig. 7: (i) upper coating/reaction layer (210-300 µm distance from the substrate-coating-interface), (ii) middle coating region (120-210 µm), and (iii) lower coating region (30-120 µm). In the lower coating region H_{IT} is between 3.0-5.3 GPa and E_{IT} is between 66-87 GPa for all the infiltrated GZO cases. It can be also seen that for all the infiltrated cases, both E_{IT} and H_{IT} values in region (ii) are higher than that of region (iii). This is due to the effect of stiffening caused by the CMAS infiltration in region (ii) which increases the E-modulus and hardness as a result. Region (iii) is mostly non-infiltrated and its H_{IT} and E_{IT} values are comparable to that of non-infiltrated coatings which remain relatively constant over the entire coating. The measured values in region (i) increase after CMAS infiltration (H_{IT}=10.9-15.6 GPa and E_{IT}=133-186 GPa).

The E_{IT} of the NI/3000 is higher than that of the NI/0 within the entire coating, while the hardness shows the opposite trend. As mentioned in section 3, no sinter bridges were formed between the GZO columns after 3000 min at 1250 °C, instead the gaps between the columns were enlarged. While at maximum test force, columns of the NI/0 sample were supported by each other, a larger displacement of the NI/3000 columns was possible due to the larger column gap. It is expected that the higher indentation depth at the same test force leads to a lower nano hardness value of the NI/3000 sample.

Both NI/0 (H_{IT}=4.0-5.7 GPa; E_{IT}=62-78 GPa) and NI/3000 (H_{IT}=3.1-4.4 GPa; E_{IT}=72-88 GPa) show lower hardness at a comparable Young's modulus than non-infiltrated (NI/300) EB-PVD 7YSZ TBCs (H_{IT}=3.7-7.5 GPa; E_{IT}=71-89 GPa) (50).

Due to the variation of infiltration depths for each CMAS/VA in GZO, there is no obvious H_{IT} or E_{IT} trend in region (ii) and (iii) with respect to the infiltration time. While infiltration led to an increase in E_{IT} and H_{IT} values, sintering of the GZO columns contributed to a higher E_{IT} and a lower H_{IT}. The different CMAS compositions showed an increase of E_{IT} and H_{IT} values in the region (ii) compared to region (iii) in the following order: C1>VA>C2. In case of CMAS 1, the infiltration of the entire region is responsible for the high mechanical properties. The limited infiltration in the region by VA followed by CMAS 2 is the reason for the lower values in H_{IT} and E_{IT}. However, in region (i), this proportion changed to VA>C2=C1. Almost all the region (i) was infiltrated for all the CMAS variants. The difference in mechanical properties arise solely due to the different reaction products and their properties, which are listed in section 3.3. The entire reaction layer of VA/3000 consists of apatite (H_{IT}=5.4 GPa; E_{IT}=71 GPa) and fluorite (H_{IT}=7.4 GPa; E_{IT}=84 GPa). Spinel (H_{IT}=8.2 GPa; E_{IT}=89 GPa) also precipitates below the first 50 µm of the reaction layer, increasing both hardness and Young's modulus between a coating thickness of 240-270 µm as shown in Fig. 7. The reaction layer of CMAS 1 and CMAS 2 is thinner, where both spinel in

13

CMAS 1 and garnet (H_{IT}=8.2-8.3 GPa; E_{IT}=77-84 GPa) in CMAS 2 are limited to the upper region of the reaction layer. Therefore, the highest measured values for both CMAS compositions are between 270-300 µm. Below that, the dominance of GZO (H_{IT}=5.4 GPa; E_{IT}=75 GPa) increases within the EB-PVD columns, leading to a slight decrease in H_{IT} and E_{IT} in both cases. Furthermore, in the upper layer region, a trend towards higher H_{IT} and E_{IT} with extended infiltration time can be observed. For example, the GZO of the VA/3000 is completely dissolved in this range, which leads to an increase in H_{IT} and E_{IT}.

4. Discussion
4.1. Impact of mechanical properties on erosion behaviour

To evaluate the influence of H_{IT} and E_{IT} on erosion behavior, the ratio H_{IT}/E_{IT} is used and this is shown in Fig. 8 H_{IT}/E_{IT} for the GZO TBCs over the entire coating, calculated from the nanoindenter data of Fig. 7. Hassani et al. [51] showed that the erosion resistance of coating systems can be positively influenced both by a high hardness (resistance to plastic deformation by particle impact) and by a low Young's modulus (avoids the brittle fracture behavior caused by elastic deformation during the initial impact of particles). To correlate the H_{IT}/E_{IT} value with the erosion behavior of the entire TBCs, the erosion data of the E/90 GZO samples from Fig. 5 d) are used. A similar discussion with E/45 is also possible considering the lower depths of the erosion spot related to the erosion time (see (50)). It can be seen that with increasing depth of the erosion spots (longer erosion time) the erosion rate increases and at the same time the H_{IT}/E_{IT} ratio decreases (region (i) to (iii). The trends of H_{IT}/E_{IT} can be correlated with characteristics of erosion trends. Hence, both VA/3000 (thick green line) and C2/300 (thin blue line) have the highest H_{IT}/E_{IT} values (Fig. 8) and the lowest erosion rates (Fig. 5 d) at the TBC surface among all GZOs. After the initial erosion phase, the erosion rates increase significantly in both cases, which is also accompanied by a rapid decrease in H_{IT}/E_{IT} at 180-210 µm. The increase in H_{IT}/E_{IT} of VA/3000 at 90 µm depth (region (iii) might be responsible for a decrease in erosion rate at about 240 s erosion time. Other examples are C1/300 and C1/3000 (thin and thick red line) where during the initial stages of erosion, both the H_{IT}/E_{IT} values and erosion rates are in the middle range among all GZO samples. Due to the constant elevated H_{IT}/E_{IT} values (Fig. 8) in region (i) and (ii), there is only a moderate increase in the erosion rate (Fig. 5 d), which results in the lowest erosion rate of all investigated infiltrated GZO TBCs after 120 s erosion time. Based on the H_{IT} and E_{IT} properties above the TBC, it was found that high hardness and a low Young's modulus have a positive effect on the erosion resistance. The H_{IT}/E_{IT} ratio serves as a guideline for the expected erosive behavior.

However, the correlation of the H_{IT}/E_{IT} ratios between infiltrated and non-infiltrated layers can only lead to limited conclusions. The high erosion rate of the NI/3000 coating (see Fig. 5) can be deduced from the lower H_{IT}/E_{IT} values among all investigated GZO TBCs (see Fig. 8). Nevertheless, in section (i) the H_{IT}/E_{IT} values of NI/0 are ca. 0.02 lower compared to the infiltrated GZO TBCs but the erosion rate of NI/0 is at least comparable to the infiltrated samples. This suggests that H_{IT}/E_{IT} ratios are not suitable for comparing the non-infiltrated EB-PVD column structures with infiltrated column structure which behaves like compact bulk material. Therefore, it is understood that as soon as the erosion mechanisms change, such as between the bulk reaction layer and the non-infiltrated EB-PVD column structure, the influence of the material properties (H_{IT}; E_{IT}) on the erosion rate is superimposed by the influence of the microstructure.
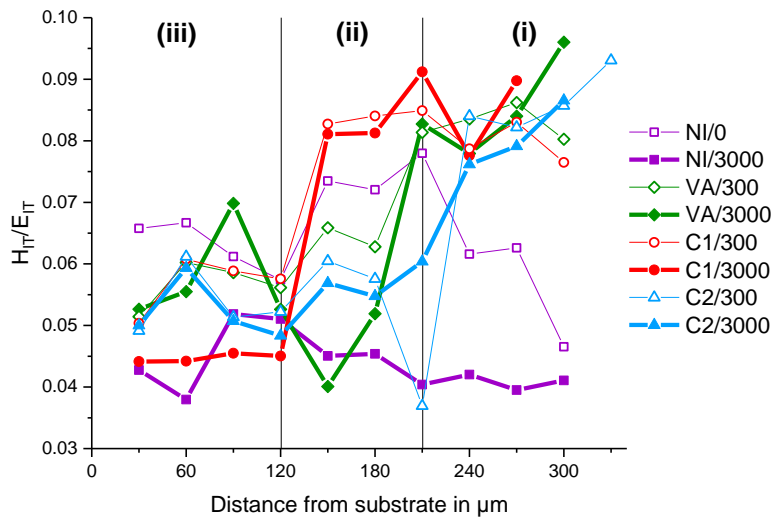
Fig. 8   The plot of H_{IT}/E_{IT} ratio calculated from data of Fig. 7 for GZO as a function of TBC thickness (starting from the substrate).

4.2. Erosion behavior of non-infiltrated GZO TBC

The columns of all GZO coatings show an inclination angle of up to 10° relative to the prevailing direction of column growth in the lower part of the coating (see Fig. 1 a). Although a negative influence of this inclination on the erosion properties can be expected, the inclination angle is below 20°, a threshold value considered critical for EB-PVD 7YSZ TBCs by Wellman et al.(39).

Due to an initial erosive impact, cracks emerge in the column tips of the NI/0, which rapidly form a network of cracks partially covered by a layer of debris (see Fig. 9 a). The formation of the layer of debris is attributed to the high intracolumnar porosity, the pronounced feather arms at the GZO column tips, and the brittle GZO material behavior. It serves as a buffer zone during particle impact. As the erosion continues, cracks develop in individual columns parallel to the coating surface and propagate over several columns in the case of too narrow column gaps (see Fig. 9 b). The newly exposed coating areas have a relatively flat coating surface due to this erosive behavior (see Fig. 10 a).

The described erosion process of the NI/0 E/90 is reflected in a gradual but successive increase of erosion rate (see Fig. 5 b). During the initial stages, the erosion rate is low due to the formation of a crack network and the debris layer. As the erosion progresses, fractured columns and narrowing gaps between the columns near the substrate cause the erosion rate to increase. A comparison of non-infiltrated GZO to non-infiltrated 7YSZ TBC is shown in (50).

Contrary to the NI/0 GZO samples, no crack network or layer of debris formed in the upper column region after 3000 min of heat treatment and subsequent erosive loading. The key factor here is the decrease in porosity along the feather arms as a result of the sintering processes (see Fig. 1 a-b). Therefore, individual columns fracture directly (see Fig. 10 b). Since the column gaps increase as a result of the sintering effects and no formation of sinter bridges can be identified, the support by the adjacent columns decreases. As a consequence, the fractured columns are removed even though the adjacent columns are not yet damaged. After erosion, the coating surface is punctuated by individual protruding columns (see Fig. 10 b). The early removal of the columns is reflected in the rapid increase of the erosion rate of the NI/3000 sample in Fig. 5 b. This lower erosion resistance compared to NI/0 can be attributed to the lower H_{IT}/E_{IT} of the NI/3000 (see Fig. 8). A comparison of the erosion behavior of the sintered NI/3000 with literature data is not feasible due to the absence of such studies.
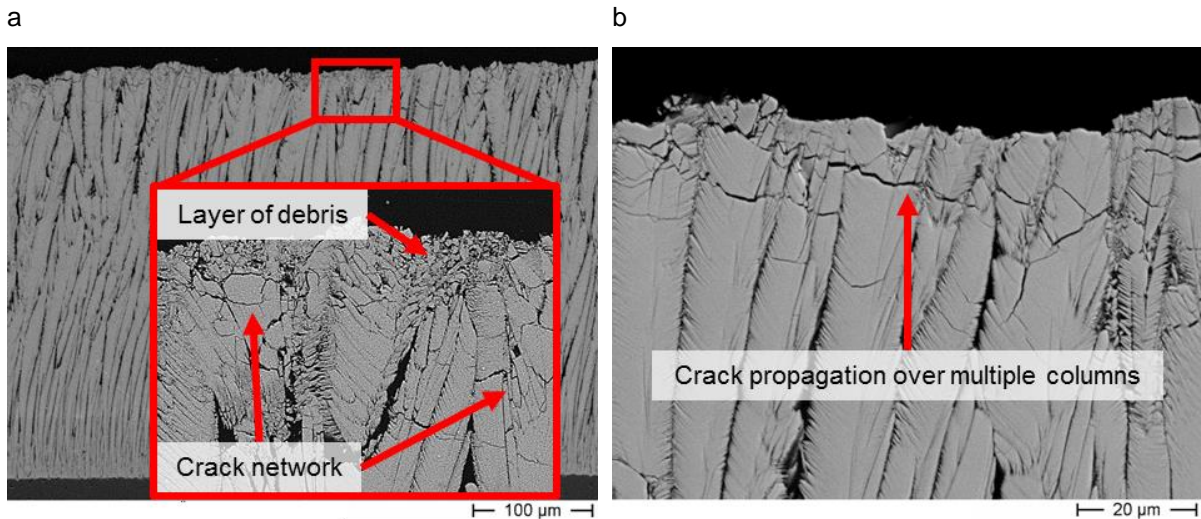
15

Fig. 9   SEM cross-sections of different erosion mechanisms of the NI/0 E/90 coating divided into a) formation of a crack network with a layer of debris above, and b) crack propagation over multiple columns due to decreasing column gaps.
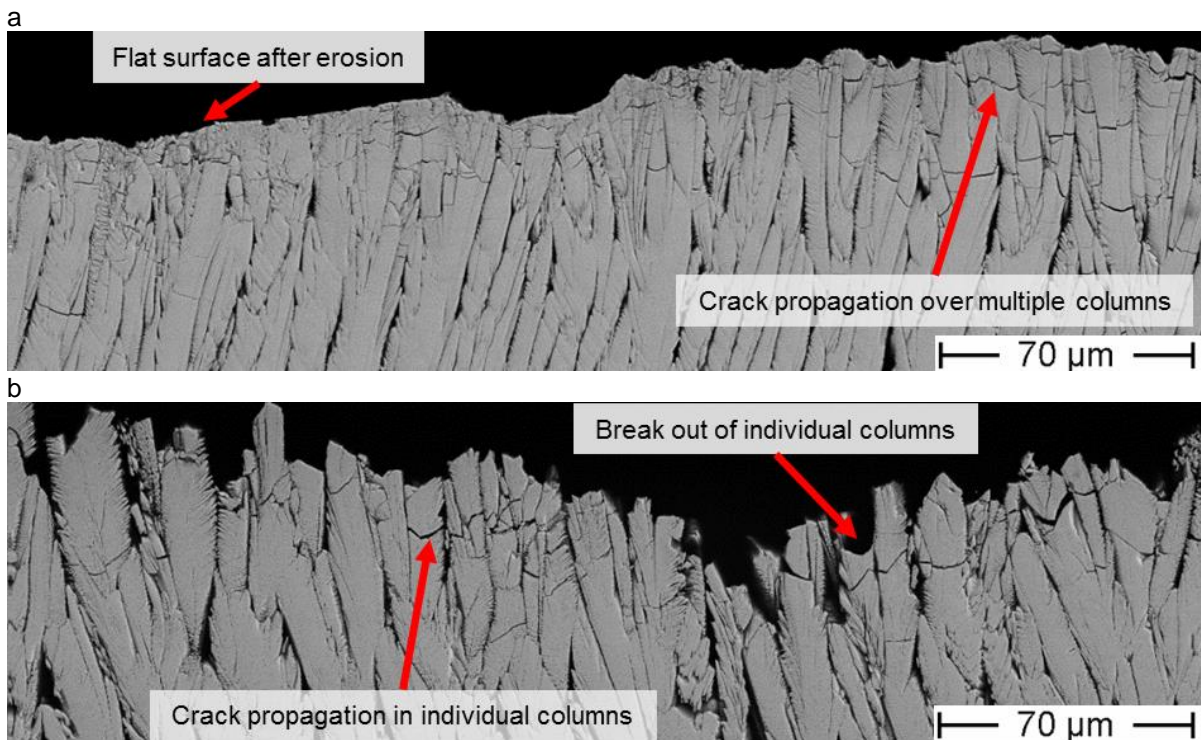

Fig. 10   SEM cross-sectional images of different surface structures of the a) NI/0 E/90 and the b) NI/3000 E/90 layers due to erosive loading.

4.3.   Erosion behavior of infiltrated GZO TBC: reaction layer and column structure

The erosion behavior of the infiltrated EB-PVD GZO coatings can be categorized into two erosion stages: (i) erosion of the reaction layer; (ii) erosion of the (subjacent) columnar structure. Due to the different reaction layers as well as the varying CMAS infiltration depths into the coating and the columns, the erosion behavior of the GZO samples is different in each erosion stage. In the following sections, the correlations of the reaction layer and infiltration depths with the erosion behavior of the GZO TBCs of selected CMAS compositions (VA, CMAS 2) and infiltration times are discussed. The gained knowledge of CMAS 1 infiltrated GZO TBC validates these results, but is omitted in order to shorten this paper. A complete discussion of all investigated CMAS-infiltrated GZO TBCs is available in (50). More information on the infiltration behavior of different CMAS compositions into the GZO coating is also presented in (50).

16

As described later in section 4.4, the E/45 tests are more sensitive in the area of the reaction layer. Therefore, the determination of the E/45 erosion properties (Fig. 5 c-d) of the reaction layer in the multi-region system and partly of the infiltrated GZO underneath the reaction layer is more precise and therefore used to correlate the erosion rate with the erosion mechanisms within the reaction layer. However, due to the 3-D Gaussian distribution of the eroding particles, the discussion of the erosion behavior of the TBC region (ii)-(iii) is mainly more accurate by using the E/90 erosion data (Fig. 5 a-b).

As already reported for infiltrated EB-PVD 7YSZ TBCs in (45), vertical cracks also form in the infiltrated GZO TBCs due to the infiltration and cooling process, which propagate through the entire coating. During erosive exposure, those cracks form an erosive weak area. This is due to the additional free surface and the missing support from the adjacent columns. However, unlike the entirely infiltrated EB-PVD 7YSZ TBCs, those cracks can also form during erosive testing when the reaction layer becomes too thin to withstand the impact of the particle. In contrast to the EB-PVD 7YSZ TBCs, the erosion resistance of GZO TBC decreased after CMAS infiltration (50).

GZO erosion behavior after a 300-minute VA infiltration at 1250 °C

After infiltration of the GZO TBCs with VA/300, the residual VA at the coating surface is interspersed with apatite needles and globular fluorite. The VA residue and the underlying fine two-phase microstructure consisting of apatite and fluorite are removed by surface erosion within the first 45 s at the center of the erosion spot. Isolated vertical cracks that extend through the entire coating lead to a local increase in material removal (see Fig. 11 a). Although the H_{IT}/E_{IT} of spinel is 0.092, which is superior to fluorite (0.088) and apatite (0.076), the column gaps in the coating region of the spinel are not completely infiltrated (see Fig. 3 a). If the erosive removal reaches the spinel inclusions, the density of the cracks increases due to the notching effect caused by the high intracolumnar porosity (non-infiltrated feather arms sealed by apatite formation) and the low H_{IT}/E_{IT} of the GZO (see Fig. 11 b and Fig. 6). Therefore, the erosion rate rises and the spinel phase in this area has no evidently positive effect on the erosion behavior. At a remaining thickness of the infiltrated coating of approx. 70 µm an increasing erosion of the infiltrated area takes place.

After removal of the uniformly infiltrated areas, the underlying non-infiltrated GZO follows the same erosion mechanisms as NI/0 despite the heat treatment of 300 min at 1250 °C. This is due to the high sintering resistance of the GZO. In contrast to E/90 (see Fig. 5), the more sensitive E/45 confirms with the converging erosion rates of 3.6 mm³/g for VA/300 compared to 3.1 mm³/g for NI/0 after 780 s.
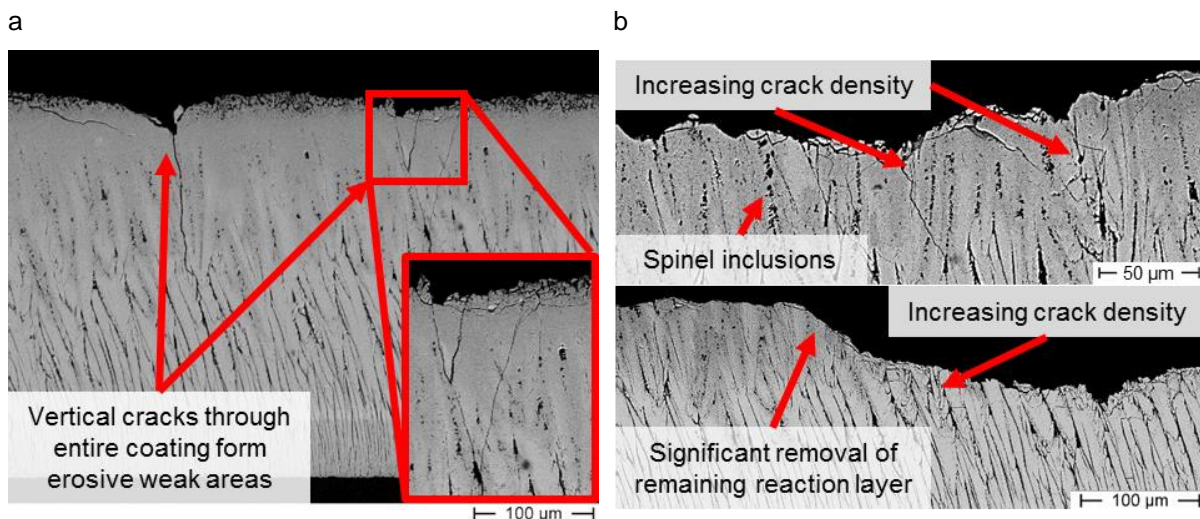

Fig. 11   SEM cross-sections of erosion regions: a) (i), b) (ii): Erosion progression and erosion mechanisms of VA/300 E/90 in the area of (a) the reaction layer, (b) the infiltrated columns.

GZO erosion behavior after 3000 min VA infiltration at 1250 °C

The VA reaction layer behaves differently after 3000 min. Although the infiltration depth is nearly the same, the reaction layer grows from 32 µm to 120 µm from 300 min to 3000 min. Both the size of the apatite needles and the fluorite grains increase significantly within the first 75 µm of the total reaction

layer. During the initial erosion phase, the VA residue is removed by the same erosion mechanisms as in case of VA/300. After removal of the VA residue above the reaction layer, crack initiation occurs in the apatite/fluorite region at an angle of up to 45° and within the remaining VA residue between the apatite/fluorite phases. Due to the higher H_{IT}/E_{IT} of the apatite phase compared to CMAS (see Fig. 6), a moderate crack deflection may occur along the apatite needles (see Fig. 12 a). The large thickness of the reaction layer leads to a reduced vertical crack density within the first 75 µm of the reaction layer and therefore to a higher erosion resistance compared to VA/300 (see Fig. 5; 0-60 s). After the removal of the acicular apatite/globular fluorite by erosion exposure, the fine two-phase apatite/fluorite microstructure with spinel inclusions meets the erodent. Subsequently, the erosive removal near the surface (see Fig. 12 b) decreases in the area of the spinel inclusions. In contrast to VA/300, the GZO columns in this area which were initially infiltrated converted in to a reaction layer after 3000 min and the elongated pores between the former feather arms are degraded within the grown reaction layer (see Fig. 3 d). Therefore, the high H_{IT}/E_{IT} ratio of spinel (see Fig. 6) affects the erosion resistance positively by crack deflection despite their local occurrence along the former column gaps. It leads to a decreasing erosion rate for VA/3000 E/45 within the first 120 s (see Fig. 5 c). After the formation of near-surface crack networks in the area of the spinel inclusions, the number of vertical cracks increases (analogous to the CMAS 1 reaction layer in (46)).

The erosion behavior of the underlying non-infiltrated coating region is comparable to the behavior of NI/3000 (see Fig. 12 b). Like the NI/3000, the erosion rates of VA/3000 increase significantly in the case of E/90. Nevertheless, they remain below the NI/3000 level due to the three-dimensional Gaussian distribution of the eroding particles in the particle stream. Owing to the multi-region (reaction layer, infiltrated GZO, non-infiltrated GZO), different layers of the VA/3000 are removed simultaneously.
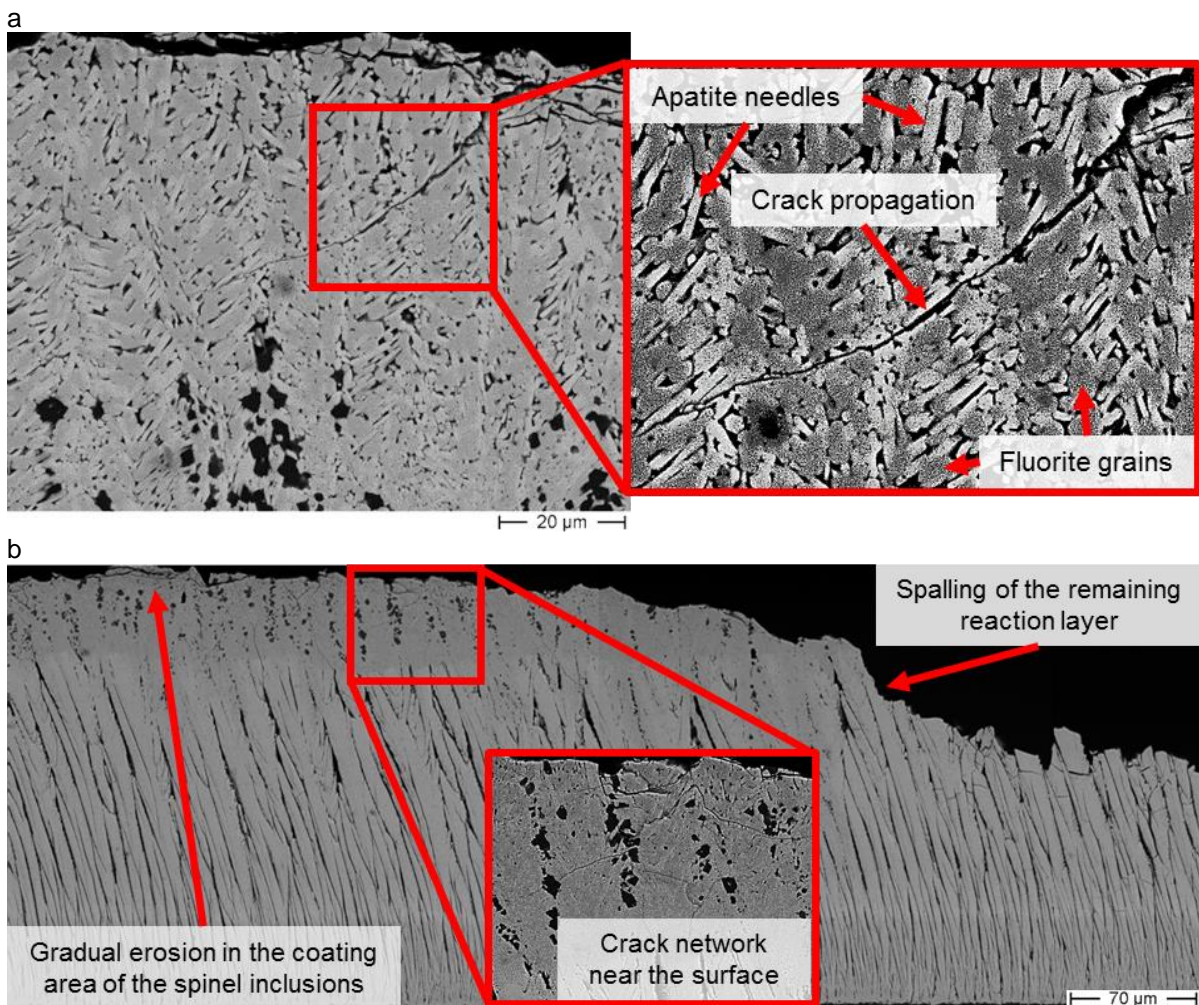

Fig. 12   SEM cross-section of erosion regions: (a) (i), (b) (i)-(ii): erosion process and erosion mechanisms of VA/3000 E/90, a) cracking in the area of pronounced apatite

18

needles/globular fluorite, b) gradual erosion of the two-phase apatite/fluorite microstructure with spinel inclusions.

GZO erosion behavior after a 300-minute CMAS 2 infiltration at 1250 °C

Reaching 2.3-3.0 mm³/g, the C2/300 GZO TBC at E/45 has the lowest initial erosion rate (0-60 s) of all 300 min infiltrated GZO samples (see Fig. 5 c). In this stage, rapid removal of the CMAS residue occurs until cracks form along the CMAS residue/garnet interface (see Fig. 13 a).

Due to the high CaO content of the CMAS, a garnet layer forms above the apatite/fluorite microstructure. The garnet growth is promoted by the constant interaction of the primary reaction products with the Mg, Al, Fe, Ti-rich CMAS 2. Based on its chemical composition $((Gd, Zr, Ca)_3(Mg, Al, Fe, Ti, Zr)_2(Si, Al, Fe)_3O_{12})$, garnet assimilates many elements of the CMAS and is therefore regarded as a sink for Mg and Fe. The thin thickness of the entire CMAS 2 reaction layer is caused by this continuous garnet layer, which inhibits ion exchange between CMAS 2 and GZO (26), since most of the Fe is bound in this garnet layer, no spinel forms below this layer.

The high nano hardness of the garnet layer of 8.3 GPa was responsible for the pronounced resistance to plastic deformation. The comparable low Young's modulus of 77 GPa reduced the tendency to brittle fracture behavior by lowering the resistance against elastic deformation. Due to the high H_{IT}/E_{IT} (see Fig. 6) and the supportive apatite/fluorite layer underneath the garnet, the garnet layer resisted erosive exposure over long durations despite its low thickness of 7 µm (see Fig. 13 a). Therefore, the garnet layer is responsible for the low erosion rate within the initial erosion phase.

After a gradual removal of the garnet by surface erosion (see Fig. 13 a), the remaining, thin apatite/fluorite reaction layer spalls off (see Fig. 13 b). The spalling leads to a rapid increase in the erosion rate for C2/300 E/45 and E/90, as shown within the first 120 s of Fig. 5 a-b. The decisive factor is the lower H_{IT}/E_{IT} of apatite and fluorite (0.076-0.088) compared to the garnet (0.108). Also, no supportive effect for the remaining 16 µm thin reaction layer can be expected from the partly infiltrated EB-PVD GZO columns underneath the reaction layer. Although CMAS 2 was able to penetrate partly into the feather arms (see Fig. 3 c), below the reaction layer the still existing elongated porosity between the former feather arms and the low H_{IT}/E_{IT} of the GZO phase within the non-infiltrated columns (see Fig. 3 c) do not provide any supportive effect during erosion. The notching effect at the pores and the cross-linking of the columns due to CMAS 2 infiltration promotes crack initiation/propagation.
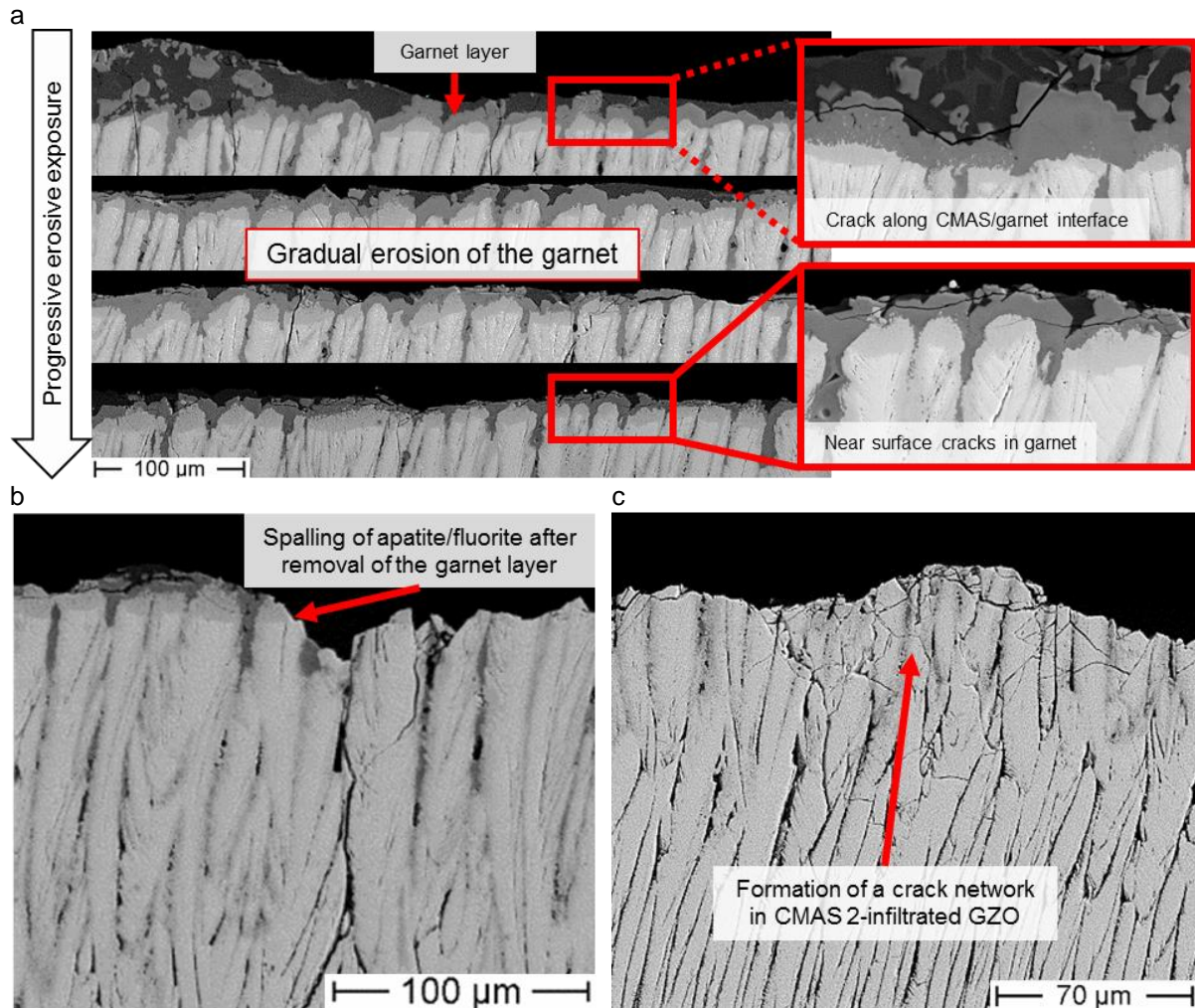
19

Fig. 13   SEM cross-sections of erosion regions: a) (i), b) (i)-(ii), c) (ii): erosion process and erosion mechanisms of C2/300 E/90, a) gradual removal of the garnet layer during a progressive erosive exposure (red dashed line indicates enlargement of a comparable area), b) spalling of the apatite/flourite reaction layer, c) formation of crack networks leads to the rapid removal of the infiltrated columnar regions.

The remaining infiltrated coating below the reaction layer is partially eroded by deeper cracks, which form crack networks with progressive erosion exposure (see Fig. 13 c). Since these extensive crack networks did not occur in other CMAS compositions, it can be assumed that the GZO TBC structure is more weakened due to the higher CaO-content in the CMAS and its associated low viscosity, as described by Ndamka (52). This hypothesis is supported by the low H_{IT} ($H_{IT\ C2/300}$=4.9 GPa) and the low E_{IT} ($E_{IT\ C2/300}$=86 GPa) at the layer thickness of 180 µm (see Fig. 7: $H_{IT\ VA/300-C1/300}$=8.4-12.5 GPa; $E_{IT\ VA/300-C1/300}$=134-148 GPa). In this phase, the erosion rate of the C2/300 E/90 sample increases significantly and reaches the level of the C2/3000 samples (see Fig. 5; 180-240 s). After the removal of the infiltrated coating, the transition to the erosive behavior of the NI/0 samples takes place, leading to a decrease of the C2/300 E/90 erosion rate.

GZO erosion behavior after a 3000-minute CMAS 2 infiltration at 1250 °C

Both the garnet phase and the apatite/fluorite reaction layer are more pronounced after C2/3000 compared to C2/300. Likewise, the infiltration depth varies between 150 µm and entire coating (50). After the CMAS residue has been eroded, there is subsequently a deeper horizontal cracking in the garnet layer compared to the C2/300 samples (see Fig. 14 a). Due to the longer infiltration time, there is an increase in the Young's modulus (E_{IT} after 300 min: 77 GPa vs. E_{IT} after 3000 min: 84 GPa), i. e. embrittlement of the garnet takes place, while the nano hardness remains unchanged (see Fig. 6). The growing apatite/flourite layer forms a diffusion barrier, which restricts the supply of Gd to the growing garnet layer, leading to a decrease of the Gd content in the garnet by about 1/3 (based on At.%). As

20

shown in our own work (26), the content of CMAS elements, e. g. Fe, Ti, Ca, increases in garnet by about 30-50 at%, while the Gd, Al and Si content decreases. It leads to an embrittlement of the garnet, which decreases its erosion resistance compared to C2/300. Due to the additional rapid removal of the reaction layer of apatite/fluorite (see Fig. 14 a), C2/3000 achieves the highest erosion rates of all infiltrated GZO TBCs in the first 120 s of the erosion test.

After the removal of the reaction layer, the infiltrated areas underneath the reaction layer are directly exposed. Due to the longer infiltration time, the elongated pores of the feather arms are disintegrated, but an increased intracolumnar porosity is formed (see Fig. 3 f). Some areas directly below the reaction layer are not infiltrated due to the wide variation in the infiltration behavior (see Fig. 2 f). While the infiltrated columns form crack networks (cf. C2/300), the non-infiltrated columns show a lower erosion resistance after 3000 min heat treatment at 1250 °C, which is comparable to the NI/3000 samples. Fig. 14 b-c shows that there is an increasing trough formation in the non-infiltrated columnar regions. The infiltrated regions enclose these troughs. Although this infiltration scenario seems to be comparable to scenario (4) in (46), in this case, there is more extensive erosion of the non-infiltrated areas. The reason for this different erosion behavior is the higher erosion rate of the non-infiltrated NI/3000 samples (E/90; 21.1 mm³/g) compared to the infiltrated C2/3000 samples (E/90; 9.8 mm³/g) (see Fig. 5). This indicates a strong reduction in the erosive resilience of the non-infiltrated microstructure as a result of extensive 3000 min lasting sinter processes compared to a CMAS 2 infiltration for 3000 min. In contrast, the non-infiltrated 7YSZ coating (3.7 mm³/g) achieves a higher erosive resistance than the CMAS 2 infiltrated 7YSZ coating after 300 min infiltration (4.8 mm³/g) (46).
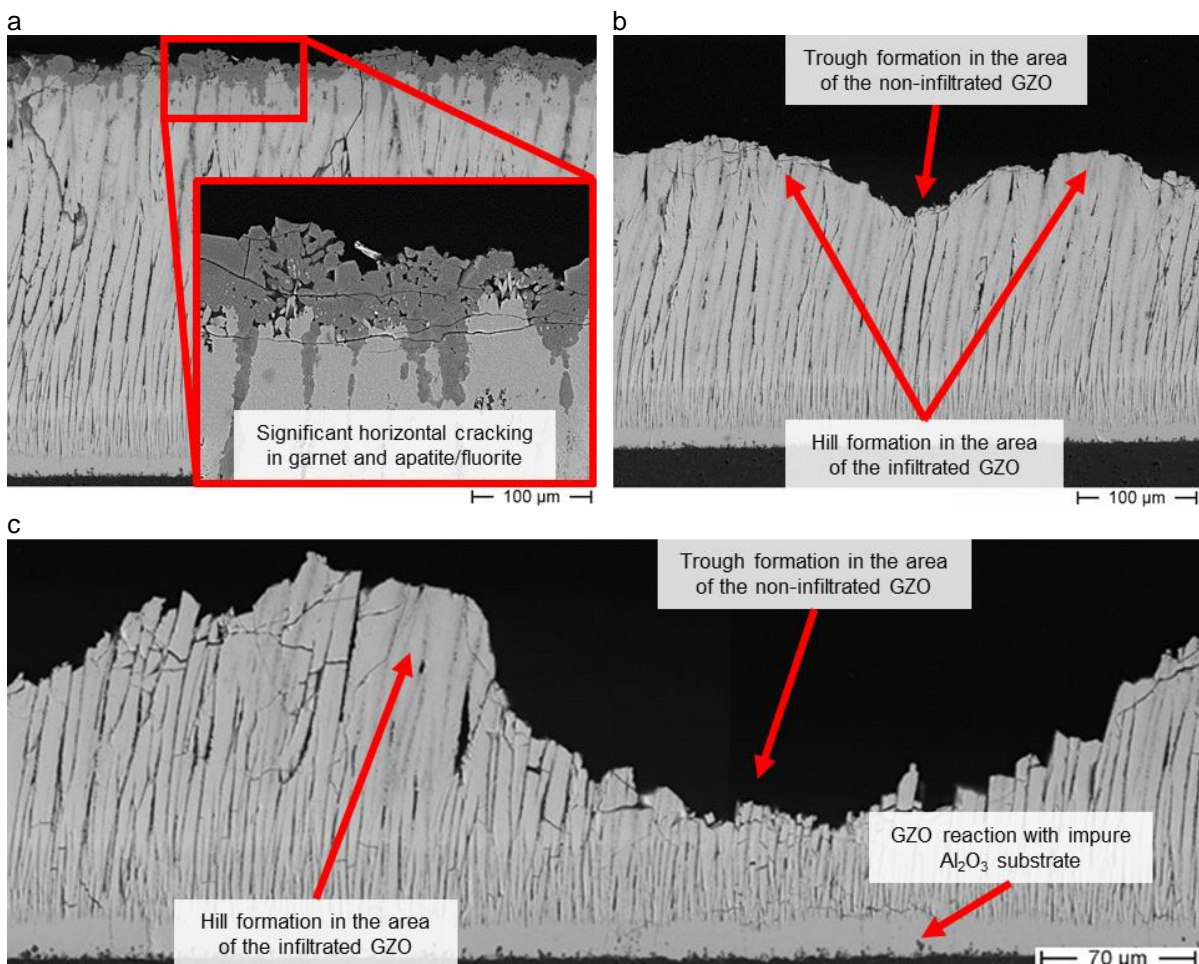

Fig. 14   SEM cross-sections of erosion regions: a) (i), b) (ii): erosion process and erosion mechanisms of the C2/3000 E/90, a) rapid erosion of the garnet layer due to intense lateral cracking, b) and c) formation of troughs due to intense removal of the non-

21

infiltrated columnar regions and formation of hills due to erosive resistant columnar regions as a result of CMAS 2 infiltration.

4.4. Erosion behavior of infiltrated GZO TBC at a particle impact of 45 °

Both the GZO material and its reaction layers are brittle in nature. It is expected for brittle materials, micro-fracturing at the near-surface (surface erosion) occurs at particle impact angles of 45° and 90°, with a higher erosion rate at 90° (see Fig. 5). The particles impacting at 45° do not transfer 100 % of their kinetic energy into the coating. Instead, the energy is shared equally between the impact energy perpendicular and the remaining particle energy tangential to the coating surface. Furthermore, a lower angle increases the size of the erosion spot, causing the particle load per area to decrease. Both aspects lead to a more gradual erosion of the individual coating areas at 45°.

In the case of CMAS-infiltrated samples, the fundamental erosion mechanism remains identical at 45° and 90°. The reaction layer of the infiltrated GZO TBCs behaves like a bulk material, whereby at 45° only the perpendicular energy component leads to near-surface cracking. The tangential energy component of the impact, on the other hand, is reflected at the surface of the coating and does not lead to any significant damage. In combination with a lower particle load per area, a delayed erosion of the individual layer areas occurs. It makes it possible to have a more precise statement on the erosion behavior of the individual reaction layers. The erosion rate of the infiltrated GZO studied under E/45 is mostly positive parabolic. The initial high erosion rate, which is partly higher than the initial erosion rate of the 90° samples, is achieved by the erosion of the highly brittle CMAS. It is removed over a larger area due to the extended size of the erosion spot. The subsequent minimum erosion rates are caused by the comparatively higher erosive resistance of the pronounced reaction layer. If a garnet layer or spinel is present within the reaction layer, the erosion resistance is positively influenced compared to the basic reaction layer (apatite/fluorite) due to the high H_{IT}/E_{IT} of the first two phases (see Fig. 6).

At 45° the lower impact energy perpendicular to the surface is not sufficient to initiate cracks in the porous column below the reaction layer. Therefore, in contrast to the samples tested at 90°, there is no spalling of the reaction layer at a remaining layer thickness of about 30 µm. Instead, continuous erosion of the remaining reaction layer takes place (see Fig. 15). Subsequently, erosion of the remaining column structure takes place, whereby the respective erosion rate in this area is strongly dependent on the infiltration level of the column structure. VA/300 E/45, for example, reaches the lowest erosion rate of all infiltrated layers after about 500 s (5.3 mm³/g), and this rate decreases further to 3.6 mm³/g until coating failure. Since the reaction layer prevented complete CMAS infiltration, the non-infiltrated column structure is comparable to NI/0 E/45 (erosion rate from 500 s to coating failure: 3.6-3.0 mm³/g) (see Fig. 5 a). Regardless of the particle impact angle, it can generally be concluded that the infiltrated GZO TBCs showed a higher erosion resistance within the first erosion stage –(i) erosion of the reaction layer– than in the subsequent erosion stage –(ii) erosion of the (underlying) column structure. In essence, the infiltration of GZO by CMAS and formation of reaction phases improves its erosion resistance by the mechanisms described above.
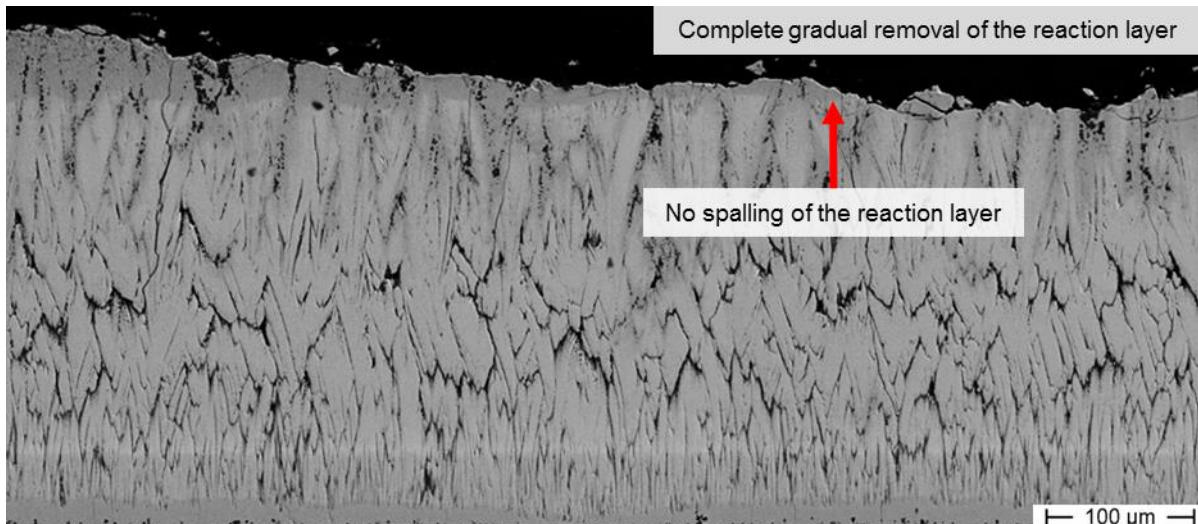
Fig. 15   Cross-section (SEM; erosion stage (i)): Image of continuous E/45 removal of the C1/3000 reaction layer without spalling. Note a small deviation between polished plane and the growing direction of the columns that has caused the unusual appearance of the GZO TBC in the lower part.

As described earlier, the general trends in erosion rates of infiltrated GZO samples at E/90 are consistent with those at E/45 concerning CMAS composition and infiltration duration. Consequently, their erosion behavior can be explained in terms of the predominant erosion mechanisms. Only the spalling of the reaction layer is less intense in E/45 because the force component of the particle perpendicular to the surface is lower compared to E/90. Thus, the measured erosion rate can be more precisely assigned to the area of the reaction layer.

4.5. Major effects and underlying mechanisms influencing erosion

The Fig. 16 summarizes the different influencing factors that led to an increase in erosion resistance described in section 4.3. These four influencing factors are explained again in more detail below.
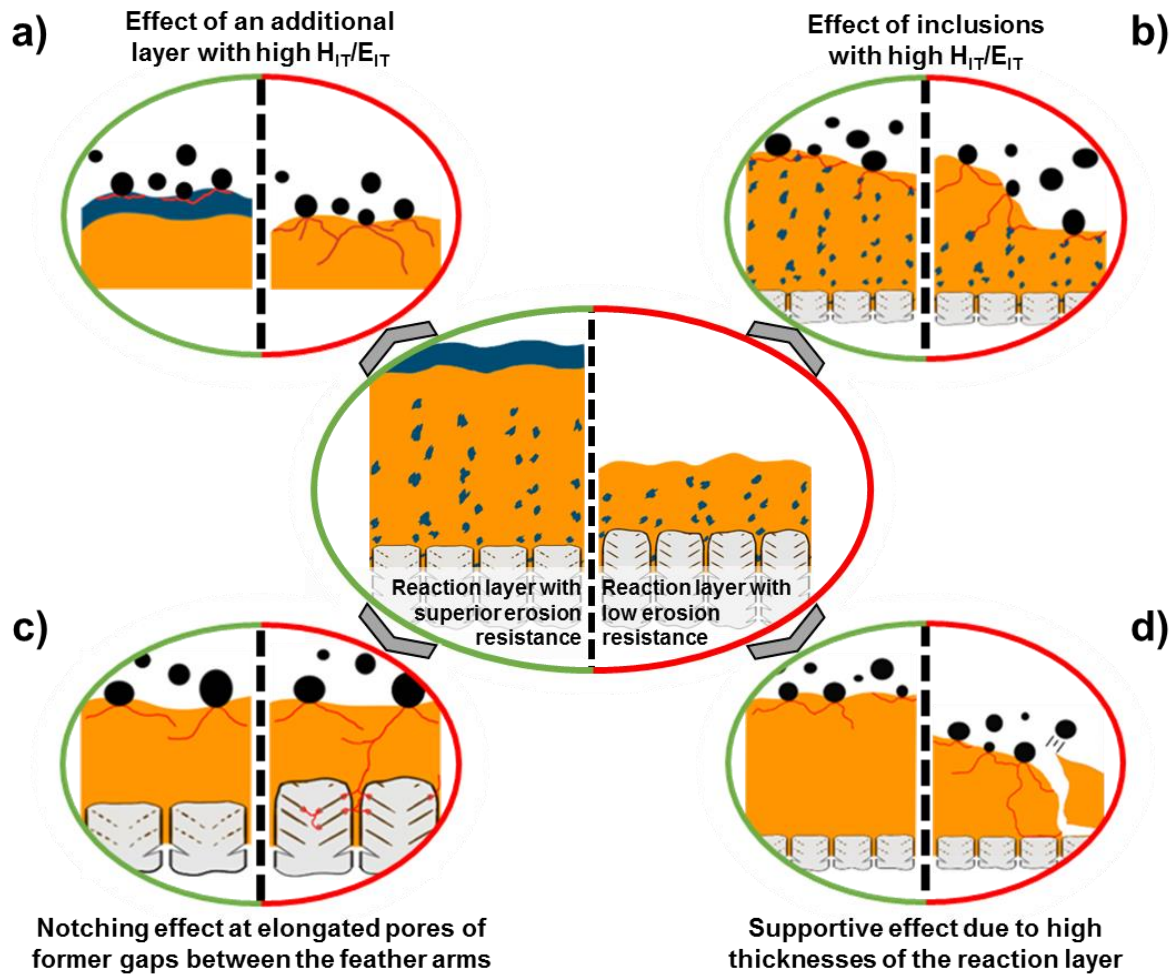
Fig. 16   Illustration of major effects to describe different influences (a-d) on the erosion resistance of the reaction layer: EB-PVD column - gray; reaction layer - orange; reaction phases with high H_{IT}/E_{IT} - dark blue; erosion particles - black. Classification of influences into positive (green) and negative (red) effects on erosion resistance based on the frame color.

In general, it has been proven that phases with high H_{IT}/E_{IT} positively influence the erosion resistance of the reaction layer. Corresponding erosion resistant phases such as garnet and spinel achieved a H_{IT}/E_{IT} that was up to 1.5 times higher than that of pure GZO. In the case of an additional layer with high H_{IT}/E_{IT} above the reaction layer (Fig. 16 a), only near-surface cracks occur within the layer, leading to reduced erosive material removal. Based on the example of the different E_{IT} values in garnet, it could be demonstrated that a lower E_{IT} positively influences the erosion resistance of such a layer. Due to the lower tendency to brittle fracture, the impulse of a particle impact can be transmitted without cracking. Without this layer, however, crack propagation occurs deep into the reaction layer. The result is a faster removal of the reaction layer.

Fig. 16 b) illustrates that due to inclusions with high H_{IT}/E_{IT} (e. g. spinel) in the TBC cracks may be deflected, depending on the angle of the crack impinging the inclusion. For this reason, in an area with multiple inclusions, single long cracks do not lead to material failure. Instead, a dense network of cracks must first develop. However, if the cracks penetrate the inclusions, then they are mostly severed. Finally, in areas of the reaction layer with no inclusions, rapid removal of the layer tends to occur, while in areas with inclusions, the removal of the layer is considerably slower.

Crack initiation within the reaction layer occurs mainly at microstructural regions with an increased notching effect, as illustrated in Fig. 16 c). Due to CMAS infiltration, the gaps between the feather arms of the EB-PVD columns are sealed, partially infiltrated, or dissolved, depending on the CMAS composition. Especially in the case of sealed gaps between the feather arms, elongated pores with a high notching effect are formed. In the case of particle erosion, these areas lead to an increased density

of cracks and finally to an elevated erosion rate due to additional crack initiation in deeper areas of the coating. However, due to prolonged CMAS infiltration, these elongated pores are degraded by penetrating CMAS and progressive sintering processes.

A particle impact generates compressive stresses in the reaction layer. In the case of an impact on a thin reaction layer, which has no underlying supportive layer, the maximum elastic/plastic deformation in the cross-section of the layer may be exceeded. In this case, it leads to vertical crack propagation throughout the reaction layer (Fig. 16 d). Subsequently, this crack continues in areas with an increased notching effect (e. g. elongated pores), in weak interfaces (e. g. with purely mechanical interlocking (46)), and erosive inappropriate mechanical properties (low H_{IT}/E_{IT} and K_{IC}). The result is a spallation of entire areas of the layer. In case of an existing supportive layer, in contrast, the elastic/plastic deformation remains a local incident at the surface of the layer, leading exclusively to near-surface cracking. The formation of a supportive layer is especially dependent on the microstructure of the TBC. For example, the inhomogeneity of the infiltration depths can be influenced via the width of the column gaps. The critical reaction layer thickness, at which vertical crack growth occurred, was ≤ 40 μm for the EB-PVD GZO and SPS Al_2O_3 reaction layers (46) during E/90 tests. 7YSZ, on the other hand, did not form a reaction layer (45). At a remaining layer thickness of about 30 μm, spalling of the remaining reaction layer occurred in both cases. However, a generally valid critical thickness of the reaction layer cannot be given due to its strong dependence on the erosion parameters (particle impact angle, velocity, shape, mass, etc.).

5. Conclusion

Erosion tests were conducted upon non-infiltrated and CMAS infiltrated $Gd_2Zr_2O_7$ EB-PVD TBCs. In contrast to the EB-PVD 7YSZ TBCs, the erosion resistance of GZO TBC decreased after CMAS infiltration. Nevertheless, after a heat treatment of comparable temperature and duration, the erosion resistance of the infiltrated TBCs exceeded those of the aged samples w/o infiltration.

Due to a CMAS infiltration, the GZO EB-PVD TBCs formed a reaction layer. Depending on the CMAS composition and infiltration time, the reaction layer differed in thickness as well as type and amount of reaction phases present in this layer. This study focused on the mechanical properties of the reaction layer and phases and their influence on the erosion behavior. It was shown that as long as no major differences in the morphology of the TBC occurred, the erosion behavior of the infiltrated TBC can be explained by the mechanical properties such as nano hardness and Young's modulus of the phases and the coating. However, these studies do not completely represent actual service conditions where a thermal gradient prevails across the coating thickness. The major difference can be expected in terms of reaction products that are formed under isothermal conditions are more uniform and continuous than that are formed under thermal gradient. Nevertheless, this study summarizes important effects in the erosion model of the reaction layers which also influence the erosion resistance of CMAS-resistant TBCs under real operating conditions.

Based on those results and the observed erosion mechanisms an erosion model of the reaction layer was developed, which highlights the following main weaknesses and strengths in the structure of reaction layers:

- A layer with a high H_{IT}/E_{IT} (i. e. garnet) on top of the apatite/fluorite reaction layer increases the initial erosion resistance by about 40 %.
- A randomly dispersed phase with high H_{IT}/E_{IT} (i. e. spinel) in the apatite/fluorite reaction layer increases its erosion resistance by about 30 % due to redirecting cracks.
- In case of no supportive layer underneath the thin reaction layer, the reaction layer tends to spall of at a thickness of around 30 μm.
- Notching effects i. e. at enclosed elongated feather arms after CMAS infiltration lead to an increased number of cracks in a deep area of the coating.

This leads to the conclusion that a TBC, which forms in case of CMAS-infiltration a reaction layer containing the combination of a garnet layer and a thick apatite/fluorite layer with spinel inclusions, would improve the erosion resistance significantly.

Additionally, the low erosion resistance in the case of an unevenly infiltrated EB-PVD structure, demonstrated in (46) was confirmed. In comparison to the unevenly infiltrated 7YSZ EB-PVD TBC in

(46) only the preferentially eroded areas changed from infiltrated to non-infiltrated areas due to different erosion rates of the individual areas.

Acknowledgments

References

1.   Padture NP. Environmental degradation of high-temperature protective coatings for ceramic-matrix composites in gas-turbine engines. npj Materials Degradation. 3 (2019). https://doi.org/10.1038/s41529-019-0075-4

2.   Darolia R. Thermal barrier coatings technology: critical review, progress update, remaining challenges and prospects. Int Mater Rev. 58 (2013) 315-48. https://doi.org/10.1179/1743280413Y.0000000019

3.   Levi CG, Hutchinson JW, Vidal-Setif MH, Johnson CA. Environmental degradation of thermal-barrier coatings by molten deposits. MRS Bulletin. 37 (2012) 932-41. https://doi.org/10.1557/mrs.2012.230

4.   Renteria AF, Saruhan B, Schulz U, Raetzer-Scheibe HJ, Haug J, Wiedemann A. Effect of morphology on thermal conductivity of EB-PVD PYSZ TBCs. Surf Coat Tech. 201 (2006) 2611-20. https://doi.org/10.1016/j.surfcoat.2006.05.003

5.   Schulz U, Raitzer-Scheibe HJ, Saruhan B, Renteria AF. Thermal conductivity issues of EB-PVD thermal barrier coatings. Materialwiss Werkst. 38 (2007) 659-66. https://doi.org/10.1002/mawe.200700189

6.   Saruhan B, Francois P, Fritscher K, Schulz U. EB-PVD processing of pyrochlore-structured La2Zr2O7-based TBCs. Surf Coat Tech. 182 (2004) 175-83. https://doi.org/10.1016/j.surfcoat.2003.08.068

7.   Schulz U, Braue W. Degradation of La2Zr2O7 and other novel EB-PVD thermal barrier coatings by CIVIAS (CaO-MgO-Al2O3-SiO2) and volcanic ash deposits. Surf Coat Tech. 235 (2013) 165-73. https://doi.org/10.1016/j.surfcoat.2013.07.029

8.   Munawar AU, Schulz U, Cerri G, Lau H. Microstructure and cyclic lifetime of Gd and Dy-containing EB-PVD TBCs deposited as single and double-layer on various bond coats. Surf Coat Tech. 245 (2014) 92-101. https://doi.org/10.1016/j.surfcoat.2014.02.047

9.   Vassen R, Traeger E, Stover D. New thermal barrier coatings based on pyrochlore/YSZ double-layer systems. International Journal of Applied Ceramic Technology. 1 (2004) 351-61.

10.   Ma W, Mack DE, Vassen R, Stover D. Perovskite-type strontium zirconate as a new material for thermal barrier coatings. Journal of the American Ceramic Society. 91 (2008) 2630-5. https://doi.org/10.1111/j.1551-2916.2008.02472.x

11.   Vassen R, Jarligo MO, Steinke T, Mack DE, Stover D. Overview on advanced thermal barrier coatings. Surf Coat Tech. 205 (2010) 938-42. https://doi.org/10.1016/j.surfcoat.2010.08.151

12.   Zhu DM, Chen YL, Miller RA. Defect clustering and nano-phase structure characterization of multi-component rare earth oxide doped zirconia-yttria thermal barrier coatings. 27th International Cocoa Beach Conference on Advanced Ceramics and Composites: A. 24 (2003) 525-34.

13.   Singh J, Wolfe DE, Miller RA, Eldridge JI, Zhu DM. Tailored microstructure of zirconia and hafnia-based thermal barrier coatings with low thermal conductivity and high hemispherical reflectance by EB-PVD. J Mater Sci. 39 (2004) 1975-85. https://doi.org/Doi 10.1023/B:Jmsc.0000017759.50800.D7

14.   Zhu DM, Miller RA. Development of advanced low conductivity thermal barrier coatings. International Journal of Applied Ceramic Technology. 1 (2004) 86-94.

15.   Drexler JM, Shinoda K, Ortiz AL, Li D, Vasiliev AL, Gledhill AD, et al. Air-plasma-sprayed thermal barrier coatings that are resistant to high-temperature attack by glassy deposits. Acta Materialia. 58 (2010) 6835-44. https://doi.org/10.1016/j.actamat.2010.09.013

16.   Clarke DR, Oechsner M, Padture NP. Thermal-barrier coatings for more efficient gas-turbine engines. MRS Bulletin. 37 (2012) 891-8. https://doi.org/10.1557/mrs.2012.232

17.   Krämer S, Yang J, Levi CG. Infiltration-Inhibiting Reaction of Gadolinium Zirconate Thermal Barrier Coatings with CMAS Melts. Journal of the American Ceramic Society. 91 (2008) 576-83. https://doi.org/10.1111/j.1551-2916.2007.02175.x

18.   Munawar AU, Schulz U, Shahid M. Microstructure and lifetime of EB-PVD TBCs with Hf-doped bond coat and Gd-zirconate ceramic top coat on CMSX-4 substrates. Surf Coat Tech. 299 (2016) 104-12. https://doi.org/10.1016/j.surfcoat.2016.05.005

19. Jackson RW, Zaleski EM, Hazel BT, Begley MR, Levi CG. Response of molten silicate infiltrated Gd2Zr2O7 thermal barrier coatings to temperature gradients. Acta Materialia. 132 (2017) 538-49. https://doi.org/10.1016/j.actamat.2017.03.081

20. Naraparaju R, Schulz U, Mechnich P, Döbber P, Seidel F. Degradation study of 7 wt.% yttria stabilised zirconia (7YSZ) thermal barrier coatings on aero-engine combustion chamber parts due to infiltration by different CaO–MgO–Al 2 O 3 –SiO 2 variants. Surface and Coatings Technology. 260 (2014) 73-81. https://doi.org/10.1016/j.surfcoat.2014.08.079

21. Nieto A, Agrawal R, Bravo L, Hofmeister-Mock C, Pepi M, Ghoshal A. Calcia–magnesia–alumina–silicate (CMAS) attack mechanisms and roadmap towards Sandphobic thermal and environmental barrier coatings. Int Mater Rev. (2020) 1-42. https://doi.org/10.1080/09506608.2020.1824414

22. David L.Poerschke RWJaCGL. Silicate Deposit Degradation of Engineered Coatings in Gas Turbines: Progress Toward Models and Materials Solutions. Annual Review of Materials Research. 47 (2017). https://doi.org/10.1146/annurev-matsci-010917105000

23. Mechnich P, Braue W, Smialek J. Solid-State CMAS Corrosion of an EB-PVD YSZ Coated Turbine Blade: Zr^{4+}Partitioning and Phase Evolution. Journal of the American Ceramic Society. 98 (2015) 296-302. https://doi.org/10.1111/jace.13241

24. Naraparaju R, Pubbysetty RP, Mechnich P, Schulz U. EB-PVD alumina (Al2O3) as a top coat on 7YSZ TBCs against CMAS/VA infiltration: Deposition and reaction mechanisms. Journal of the European Ceramic Society. 38 (2018) 3333-46. https://doi.org/10.1016/j.jeurceramsoc.2018.03.027

25. Gomez Chavez JJ, Naraparaju R, Mechnich P, Kelm K, Schulz U, Ramana CV. Effects of yttria content on the CMAS infiltration resistance of yttria stabilized thermal barrier coatings system. Journal of Materials Science & Technology. 43 (2020) 74-83. https://doi.org/10.1016/j.jmst.2019.09.039

26. Chavez JJG, Naraparaju R, Mikulla C, Mechnich P, Kelm K, Ramana CV, et al. Comparative study of EB-PVD gadolinium-zirconate and yttria-rich zirconia coatings performance against Fe-containing calcium-magnesium-aluminosilicate (CMAS) infiltration. Corrosion Science. 190 (2021). https://doi.org/10.1016/j.corsci.2021.109660

27. Viswanathan V, Dwivedi G, Sampath S, Faber K. Multilayer, Multimaterial Thermal Barrier Coating Systems: Design, Synthesis, and Performance Assessment. Journal of the American Ceramic Society. 98 (2015) 1769-77. https://doi.org/10.1111/jace.13563

28. Krause AR, Garces HF, Dwivedi G, Ortiz AL, Sampath S, Padture NP. Calcia-magnesia-alumino-silicate (CMAS)-induced degradation and failure of air plasma sprayed yttria-stabilized zirconia thermal barrier coatings. Acta Materialia. 105 (2016) 355-66. https://doi.org/10.1016/j.actamat.2015.12.044

29. Naraparaju R, Gomez Chavez JJ, Schulz U, Ramana CV. Interaction and infiltration behavior of Eyjafjallajökull, Sakurajima volcanic ashes and a synthetic CMAS containing FeO with/in EB-PVD ZrO 2 -65 wt% Y 2 O 3 coating at high temperature. Acta Materialia. 136 (2017) 164-80. https://doi.org/10.1016/j.actamat.2017.06.055

30. Mikulla C, R.Naraparaju, U.Schulz, Toma L, barbosa M, C.Leyens. Investigation of CMAS Resistance of Sacrificial Suspension Sprayed Alumina Topcoats on EB-PVD 7YSZ Layers. 2019.

31. Mikulla C, Naraparaju R, Schulz U, Toma FL, Barbosa M, Steinberg L, et al. Investigation of CMAS Resistance of Sacrificial Suspension Sprayed Alumina Topcoats on EB-PVD 7YSZ Layers. Journal of Thermal Spray Technology. 29 (2020) 90-104. https://doi.org/10.1007/s11666-019-00951-4

32. Poerschke DL, Barth TL, Fabrichnaya O, Levi CG. Phase equilibria and crystal chemistry in the calcia-silica-yttria system. Journal of the European Ceramic Society. 36 (2016) 1743-54. https://doi.org/10.1016/j.jeurceramsoc.2016.01.046

33. Mechnich P, Braue W, Green DJ. Volcanic Ash-Induced Decomposition of EB-PVD $Gd_2Zr_2O_7$Thermal Barrier Coatings to Gd-Oxyapatite, Zircon, and Gd,Fe-Zirconolite. Journal of the American Ceramic Society. 96 (2013) 1958-65. https://doi.org/10.1111/jace.12251

34. Wellman RG, Nicholls JR, Murphy K. Effect of microstructure and temperature on the erosion rates and mechanisms of modified EB PVD TBCs. Wear. 267 (2009) 1927-34. https://doi.org/10.1016/j.wear.2009.04.002

35. Mercer C, Williams JR, Clarke DR, Evans AG. On a ferroelastic mechanism governing the toughness of metastable tetragonal-prime (t ') yttria-stabilized zirconia. P R Soc A. 463 (2007) 1393-408. https://doi.org/10.1098/rspa.2007.1829

36. Schmitt MP, Rai AK, Bhattacharya R, Zhu DM, Wolfe DE. "Multilayer thermal barrier coating (TBC) architectures utilizing rare earth doped YSZ and rare earth pyrochlores". Surf Coat Tech. 251 (2014) 56-63. https://doi.org/10.1016/j.surfcoat.2014.03.049

37. Schmitt MP, Stokes JL, Gorin BL, Rai AK, Zhu DM, Eden TJ, et al. Effect of Gd content on mechanical properties and erosion durability of sub-stoichiometric Gd2Zr2O7. Surf Coat Tech. 313 (2017) 177-83. https://doi.org/10.1016/j.surfcoat.2016.12.045

38.   Mahade S, Curry N, Bjorklund S, Markocsan N, Nylen P, Vassen R. Erosion Performance of Gadolinium Zirconate-Based Thermal Barrier Coatings Processed by Suspension Plasma Spray. Journal of Thermal Spray Technology. 26 (2017) 108-15. https://doi.org/10.1007/s11666-016-0479-4

39.   Wellman RG, Nicholls JR. The effect of TBC morphology on the erosion rate of EB PVD TBCs. Wear. 258 (2005) 349-56. https://doi.org/10.1016/j.wear.2004.04.011

40.   Wellman RG, Nicholls JR. Erosion, corrosion and erosion-corrosion of EB PVD thermal barrier coatings. Tribol Int. 41 (2008) 657-62. https://doi.org/10.1016/j.triboint.2007.10.004

41.   Wellman RG, Nicholls JR. A review of the erosion of thermal barrier coatings. J Phys D Appl Phys. 40 (2007) R293-R305. https://doi.org/10.1088/0022-3727/40/16/R01

42.   Cernuschi F, Guardamagna C, Capelli S, Lorenzoni L, Mack DE, Moscatelli A. Solid particle erosion of standard and advanced thermal barrier coatings. Wear. 348 (2016) 43-51. https://doi.org/10.1016/j.wear.2015.10.021

43.   Rezanka S, Mack DE, Mauer G, Sebold D, Guillon O, Vaßen R. Investigation of the resistance of open-column-structured PS-PVD TBCs to erosive and high-temperature corrosive attack. Surface and Coatings Technology. (2017). https://doi.org/10.1016/j.surfcoat.2017.05.003

44.   Jackson RW, Zaleski EM, Poerschke DL, Hazel BT, Begley MR, Levi CG. Interaction of molten silicates with thermal barrier coatings under temperature gradients. Acta Materialia. 89 (2015) 396-407. https://doi.org/10.1016/j.actamat.2015.01.038

45.   Steinberg L, Naraparaju R, Heckert M, Mikulla C, Schulz U, Leyens C. Erosion behavior of EB-PVD 7YSZ coatings under corrosion/erosion regime: Effect of TBC microstructure and the CMAS chemistry. Journal of the European Ceramic Society. 38 (2018) 5101-12. https://doi.org/10.1016/j.jeurceramsoc.2018.06.039

46.   Steinberg L, Mikulla C, Naraparaju R, Toma F-L, Großmann H, Schulz U, et al. Erosion resistance of CMAS infiltrated sacrificial suspension sprayed alumina top layer on EB-PVD 7YSZ coatings. Wear. 438-439 (2019) 203064. https://doi.org/10.1016/j.wear.2019.203064

47.   Naraparaju R, Mechnich P, Schulz U, Rodriguez GCM. The Accelerating Effect of CaSO4 Within CMAS (CaO-MgO-Al2O3-SiO2) and Its Effect on the Infiltration Behavior in EB-PVD 7YSZ. Journal of the American Ceramic Society. 99 (2016) 1398-403. https://doi.org/10.1111/jace.14077

48.   Naraparaju R, Lau H, Lange M, Fischer C, Kramer D, Schulz U, et al. Integrated testing approach using a customized micro turbine for a volcanic ash and CMAS related degradation study of thermal barrier coatings. Surf Coat Tech. 337 (2018) 198-208. https://doi.org/10.1016/j.surfcoat.2018.01.030

49.   Rivera-Gil MA, Gomez-Chavez JJ, Ramana CV, Naraparaju R, Schulz U, Muñoz-Saldaña J. High temperature interaction of volcanic ashes with 7YSZ TBC's produced by APS: Infiltration behavior and phase stability. Surface and Coatings Technology. 378 (2019) 124915. https://doi.org/10.1016/j.surfcoat.2019.124915

50.   Steinberg L. Untersuchung des erosiven Verhaltens von Wärmedämmschichten nach CaO-MgO-Al2O3-SiO2 Infiltration: TU Dresden; 2021.

51.   Hassani S, Klemberg-Sapieha JE, Bielawski M, Beres W, Martinu L, Balazinski M. Design of hard coating architecture for the optimization of erosion resistance. Wear. 265 (2008) 879-87. https://doi.org/10.1016/j.wear.2008.01.021

52.   Craig M, Ndamka NL, Wellman RG, Nicholls JR. CMAS degradation of EB-PVD TBCs: The effect of basicity. Surface and Coatings Technology. 270 (2015) 145-53. https://doi.org/10.1016/j.surfcoat.2015.03.009